

Contents

1	Introduction	1
2	Physics of cosmic rays	3
2.1	History	3
2.2	Acceleration	4
2.2.1	Diffusive shock acceleration (Fermi I)	4
2.2.2	Stochastic scattering acceleration (Fermi II)	5
2.2.3	Centrifugal acceleration in rotating \vec{B} -fields	5
2.2.4	Direct electrostatic acceleration	6
2.2.5	Other types & general classification	6
2.2.6	Acceleration of uncharged particles	7
2.3	Propagation	8
2.3.1	Intergalactic propagation & transport equation	8
2.3.2	Extragalactic propagation & GZK-Cutoff	10
2.4	Composition	11
2.5	Energy spectrum	11
3	Extensive air showers	15
3.1	Electromagnetic showers	15
3.2	Hadronic showers	17
3.3	Composite primaries	18
3.4	Comments on validity	19
3.5	Detection methods	20
3.5.1	Cherenkov light	20
3.5.2	Fluorescence	21
3.5.3	Radio Emission	22
4	The Pierre Auger Observatory	23
4.1	Fluorescence Detector (FD)	23
4.2	Surface Detector (SD)	25
4.2.1	Data acquisition (DAQ)	25
4.2.2	<u>Offline</u> calibration	26
4.2.3	Online calibration	30
4.3	Event Reconstruction	30
4.3.1	Trigger procedure	31
4.3.2	Core position	32
4.3.3	Arrival direction	32
4.3.4	Energy estimation	33
4.3.5	Primary particle	34

5 Neural networks	35
5.1 Dense neural network	35
5.2 Convolutional neural network	36
5.3 Recurrent neural network	36
5.4 Other architectures	38
6 Neural network training data	39
6.1 Background dataset	39
6.1.1 Accidental muons	39
6.1.2 Electronic noise	40
6.1.3 Random traces	41
6.2 Signal dataset	45
6.3 Trace building	45
6.3.1 Filtering and downsampling	46
6.3.2 Sliding window analysis & Labelling	48
7 Classical station triggers	49
7.1 Implementation	49
7.1.1 Threshold trigger (Th)	49
7.1.2 Time over Threshold trigger (ToT)	50
7.1.3 Time over Threshold deconvoluted trigger (Totd)	51
7.1.4 Multiplicity of Positive Steps (MoPS)	51
7.2 Performance	52
7.2.1 Lateral Trigger Probability function	52

1 Introduction

TODO

CR mass extinction pleistocene

2 Physics of cosmic rays

The term cosmic ray is used in the context of particles that travel through space close to the speed of light. Their kinetic energy far exceeds their rest mass, and ranges from $O(\text{GeV})$ for solar particles to energies exceeding 10^{20}eV for atoms of extragalactic origin. The latter are typically referred to as **Ultra High Energy CRs (UHECRs)** in literature.

This chapter aims to introduce the general physical principles needed to describe cosmic rays. For this purpose, an overview of the origin of CRs is presented in section 2.2, discussions regarding their propagation in space, the resulting primary and energy composition are given in section 2.3, section 2.4 and section 2.5 respectively. Immediately following is a summary of the discovery of cosmic rays in section 2.1.

2.1 History

A first hint at the existence of high-energy particles in the upper atmosphere was given by Hess in 1912, who found that the discharge rate of an electroscope is altitude-dependant. Millikan coined the term cosmic "rays" for these particles, as he argued the ionizing radiation must be part of the electromagnetic spectrum [1]. This was later, at least partially, falsified with the discovery of the east-west effect [2]. Hess' observation however withstood the tests of time and was ultimately recognized with the Nobel prize in physics in 1936 [3]. Two years later, in 1938, Pierre Auger showed via coincidence measurements that cosmic rays in fact originate from outer space, and gave a first description of extensive air showers [4]. Another 60 years later, the Pierre Auger collaboration would adopt his experimental setup and name in their search for cosmic rays of the highest energies.

In the meantime, numerous results from different cosmic ray detectors all over the globe have helped propel the related fields of particle physics, astro physics and cosmology to new insights. Observations from cosmic ray physics serve as a valuable cross-check to the hadronic interaction models developed e.g. at CERN [5]. New theories modeling the final moments in the life of stars have arisen thanks to results from e.g. Kamiokande [6]. Last but not least, publications by the Pierre Auger collaboration regarding the CR energy spectrum and flux help refine knowledge of our cosmic neighbourhood [7, 8].

2.2 Acceleration

Following the detection of a cosmic ray on earth, the logically following questions are "where did it originate from?", and "how was it accelerated?". It is clear that particles with extreme energies must be created under extreme conditions. In particular regions with large electromagnetic (EM) fields, either in field strength or spatial extent, play a big role in the acceleration of CRs for reasons listed in the following pages. Several acceleration mechanisms have been identified.

2.2.1 Diffusive shock acceleration (Fermi I)

Super Nova Remnants (SNR) typically feature a plasma sphere propagating outwards from the former stars core into the Inter Stellar Medium (ISM), in this region of plasma any magnetic field lines will be comoving, according to Alfvén's theorem [9]. First realised by Fermi, such SNR shock fronts serve as source of high-energy CRs [10].

If a low-energy particle is injected into the SNR shock front, it will eventually be reflected by the local \vec{B} -field. If the diffusion length within the plasma is much smaller than the spatial extent of the SNR, the shock front can be modelled as a plane, and the process is analogous to an elastic reflection against a wall. Consequently, if $\frac{d\vec{B}}{dt} = 0$, this does not cause the particle to gain any energy, especially because $W = \vec{F}_L \cdot \vec{r} \propto (\vec{v} \times \vec{B}) \cdot \vec{r} = 0$. However, because the \vec{B} -field is moving radially outward alongside the plasma, a net energy gain of

$$\Delta E = +\beta_{\text{SNR}} \cdot E_0 \quad (2.1)$$

arises, where $\beta_{\text{SNR}} = |\vec{v}_{\text{SNR}}| / c$ and E_0 are the velocity of the shock-front and the initial energy of the particle. From chapter 7 in [10] it follows that ionization losses within the shock front are not completely negligible. Hence a particle must have a sufficient energy such that ΔE in Equation 2.1 exceeds possible ionization losses. The corresponding threshold for the primary energy above which acceleration occurs is dubbed the injection energy, and is of the order of 200 MeV for protons.

Furthermore, because typically $\beta_{\text{SNR}} \leq 0.10$ a single acceleration cycle is not enough to explain the CR energies observed on earth. Instead, multiple cycles are needed. This requires additional, focusing \vec{B} -fields, provided for example by the ISM, which alter the trajectory of injected particles such that they can be reflected off the shock-front again.

With each cycle, the particles rigidity $R = |\vec{p}|c / q$ increases, until its gyroradius $\rho = R/|\vec{B}|$ exceeds the spatial extent of the focusing \vec{B} -field and the particle escapes into space. With an effective ejection probability p per cycle, the energy after n cycles and the expected flux w.r.t energy, $\Phi(E)$, becomes roughly

$$E(n) = E_0 (1 + \beta_{\text{SNR}})^n. \quad (2.2)$$

$$\begin{aligned}
N(n) &= N_0 (1 - p)^n \\
\Leftrightarrow \log \left(\frac{N(n)}{N_0} \right) &= n \cdot \log (1 - p) \\
\Leftrightarrow \stackrel{(2.2)}{=} \log \left(\frac{E(n)}{E_0} \right) &\frac{\log(1-p)}{\log(1+\beta_{\text{SNR}})} \\
\Leftrightarrow N(E) &= N_0 \cdot \left(\frac{E(n)}{E_0} \right)^{\log(1-p) / \log(1+\beta_{\text{SNR}})} \\
\Rightarrow \Phi(E) &= \frac{dN}{dE} \propto E(n)^{\alpha-1}, \tag{2.3}
\end{aligned}$$

where $\alpha = \frac{\log(1-p)}{\log(1+\beta_{\text{SNR}})}$ in Equation 2.3 is a spectral coefficient whose exact value will depend on the age of the SNR (β_{SNR} decreases with age), the injected particle (different primaries have different injection energies and ejection probabilities), as well as many other factors that are often not known a priori. It can however be observed that the expected spectrum is a power law in the ranges from injection energy to a cutoff at the highest energies, which arises due to the finite lifetime of SNRs.

Results from several studies (e.g. [8, 11, 12]) hint that the presented first order Fermi acceleration mechanism is the main source of galactic CRs, extrasolar particles that originate from within the milky way, with energies ranging up to orders $O(\text{TeV})$.

2.2.2 Stochastic scattering acceleration (Fermi II)

Second order (or stochastic) Fermi acceleration is the more general case of subsection 2.2.1 and represents the original idea developed by Fermi in [10]. The underlaying principle of scattering particles off plasma clouds remains unchanged. However, if the diffusion length within the cloud exceeds its radius of curvature, the energy gain per collision instead becomes

$$\Delta E \propto + (\beta_{\text{SNR}})^2 \cdot E_0. \tag{2.4}$$

Logically, this represents a much more inefficient acceleration mechanism, but is nevertheless observed in nature under certain circumstances (c.f. [13]).

2.2.3 Centrifugal acceleration in rotating \vec{B} -fields

Some astrophysical objects such as pulsars or Active Galactic Nuclei (AGNs) possess strong magnetic fields ranging from 1 T for some AGNs [14] to ≈ 10 GT for magnetars, a subset of pulsars with extremely high magnetic flux densities [15].

If such objects rotate at an angular velocity Ω , which is in general nonzero, charged particles at a radial distance r from the rotation axis will undergo centrifugal acceleration. In particular, their Lorentz factor γ behaves like Equation 2.5 [16].

$$\gamma := \frac{E}{m_0 c^2} = \frac{\gamma_0}{1 - \left(\frac{\Omega r}{c}\right)^2}, \quad (2.5)$$

where m_0 is the rest mass of the particle and γ_0 the prior Lorentz factor before acceleration. It follows that a test particle can in theory gain an arbitrarily high energy from this process by outspiraling towards the light cylinder surface, where $\Omega \cdot r = c$. In reality however, these processes are stopped by e.g. inverse Compton scattering at some point [17]. In any case, [16] and [17] conclude that values of $\gamma \approx 10^7 - 10^8$ are possible, corresponding to protons at $\approx 10 \text{ PeV} - 10 \text{ PeV}$ or iron nuclei at $\approx 500 \text{ PeV} - 5 \text{ EeV}$ energy.

2.2.4 Direct electrostatic acceleration

The presence of non-static \vec{B} -fields implies the existence of (in vacuum) comparably strong \vec{E} -fields and a corresponding electrical potential difference Φ across different regions within the magnetosphere. A back-of-the-envelope calculation reveals that they are (neglecting constant factors) proportional to

$$|\vec{E}| \propto \frac{\Omega r_0}{c} \cdot |\vec{B}|, \quad (2.6)$$

$$\Phi \propto r_0 \cdot |\vec{E}|, \quad (2.7)$$

where r_0 is the radius of the central object rotating at an angular frequency Ω . Consequently, an ion with atomic number Z can be accelerated to energies $E = Z \cdot e \cdot \Phi$, which can in some cases easily exceed 10^{20} eV [18].

Some caveats to this consideration need to be mentioned. Screening effects from plasma clouds surrounding the central body are expected to limit the electrical field strength, and maximum acceleration energy by extension. Additionally, losses via e.g. Bremsstrahlung have been neglected in the above calculation, limiting the maximum attainable energy in theory even further.

2.2.5 Other types & general classification

Several acceleration mechanisms have been discussed. A plethora of other interactions that are able to accelerate elementary particles to fantastic energies remain unmentioned, or even undiscovered, as CR physics is an active area of research. In general though the driving force behind all considered (and non-considered) acceleration mechanisms are thought to be (electro-) magnetic fields, given their infinite range and large coupling strengths compared to other fundamental forces. Consequently, the maximum energy

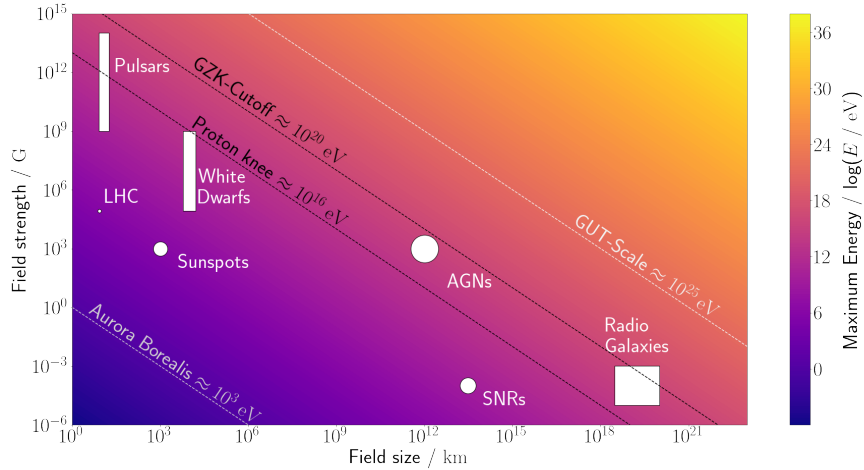


Figure 2.1: Rough estimate of field strength and size of different CR sources as well as the corresponding maximum energy estimated with Equation 2.8 ($\beta = Z = 1$). Isoenergetic lines mark notable points in the energy spectrum discussed in section 2.5.

a specific CR accelerator with magnetic field \vec{B} and size L moving at velocity βc can in theory provide for a particle with charge Ze is given by the Hillas formula [19]:

$$E_{\max} [\text{PeV}] = |\vec{B}| [\mu\text{G}] \cdot L [\text{pc}] \cdot Z \cdot \beta \quad (2.8)$$

This allows for an elegant classification of different cosmic ray sources, in part discussed on the previous pages, according to the Hillas plot shown in Figure 2.1.

2.2.6 Acceleration of uncharged particles

Particles like neutrons, neutrinos or photons possess no electromagnetic charge $q = 0$. Assuming Equation 2.8 holds in these cases, they should thus not appear in the CR spectrum. This is in disagreement with reality, where energies from 100 GeV up to ≈ 100 EeV have been observed [20, 21]. Consequently, additional interaction channels are required to explain the existence of such uncharged CRs.

High energy γ -rays in particular can be created by accelerated, charged particles via Bremsstrahlung. This occurs for example during centrifugal acceleration near pulsars or AGNs (compare subsection 2.2.3). Furthermore, inverse Compton scattering with a high-energy cosmic ray can imply a significant energy gain for a photon [22].

Uncharged CRs are also frequently produced in nuclear interactions, such as e.g. deeply inelastic scattering of charged CRs with the ISM. This especially contributes to the CR photon spectrum, as high energy π^0 are often byproducts of such scattering processes. The uncharged pions then decay into two photons. Furthermore, neutrons or neutrinos can originate from interactions involving the weak force. When a proton converts

to $p \rightarrow n + e^+ + \bar{\nu}_e$ during the decay of a UHECR ion, the resulting decay products, positron, neutron and electron-antineutrino inherit the parents' energy, and are thus high energy cosmic rays as well.

2.3 Propagation

Once a cosmic ray has been observed coming from some arrival direction (ϕ, θ) , backtracking its' trajectory to an eventual origin is, ignoring external factors, in the literal sense, straight forward. It has been shown however that several effects need to be considered for an accurate treatment of CR propagation.

For uncharged CRs (γ, n), this task is simple. Such particles are not deflected by cosmic \vec{E} and \vec{B} -fields. Possible interactions either demand the destruction of the particle (pair production, weak decay), or occur close to the source (e.g. Compton scattering), in which case the observed arrival direction will still be coincident with the actual source [23]. Gravitational lensing effects in some cases alter the trajectory of extragalactic photons. Such phenomena (if present in the first place) are however well understood in the scope of general relativity, and can be corrected for [24, 25].

2.3.1 Intergalactic propagation & transport equation

Contrary, charged particles (e^\pm, p , ions) propagate along non-trivial paths within galaxies due to deflections from solar- and galactic EM-fields. While the galactic field is coherent over large scales, numerous irregular magnetic domains, seeded in part by individual stars complicate CR propagation to essentially a three-dimensional random walk [26]. It is thus challenging to pinpoint the origin of a charged cosmic ray.

Nevertheless, related queries, such as for example the question whether or not a particle of given energy is likely to be of extragalactic origin can be answered by examining the distribution of cosmic rays within a region of spacetime. The behaviour of a population of n_i particles of type i can be approximately recreated via the below transport equation:

$$\frac{\partial n_i}{\partial t} = \underbrace{Q_i}_{\text{Source}} + \underbrace{\nabla D_i (\nabla n_i)}_{\text{Diffusion}} - \underbrace{\frac{\partial k_i(E)}{\partial E}}_{\text{Energy}} - \underbrace{\left(\frac{n_i}{\tau_{\text{spal.}, i}} - \sum_{j>i} \frac{n_j p_{ij}}{\tau_{\text{spal.}, j}} \right)}_{\text{Spallation}} - \underbrace{\left(\frac{n_i}{\tau_{\text{rad.}, i}} - \sum_{j>i} \frac{n_j d_{ij}}{\tau_{\text{rad.}, j}} \right)}_{\text{Weak decay}}$$

- **Source Q_i :**

The source term is responsible for the creation of CR particles (of type i). The exact form of Q_i will depend on the considered creation process. For example, the near instantaneous creation of n_γ photons in a Gamma-Ray Burst (GRB) at time t_0 and location \vec{r}_0 can be modelled like $Q_\gamma = n_\gamma \delta(\vec{r} - \vec{r}_0) \delta(t - t_0)$.

- **Diffusion** $\nabla D_i (\nabla n_i)$:

The random walk mentioned above is accounted for in the diffusion term, which takes a similar form to the Stokes-Einstein equation. The diffusion coefficient(s) D_i in the most general case take a tensor form due to anisotropic diffusion in different directions. Furthermore, D_i is different for each particle type, as the deflecting EM-fields couple to the respective charges q_i , which need not be equal in principle.

- **Energy loss** $\partial k_i(E) / \partial E$:

During propagation, a cosmic ray can interact with the ISM, and lose energy in the process. If this happens often enough, the CR is eventually thermalized and does not contribute to the population i any longer. Different interaction channels for different CR types i require different loss models $k_i(E)$ for each type.

- **Spallation** $(n_i / \tau_{\text{spal.}, i} - \sum n_j p_{ij} / \tau_{\text{spal.}, j})$:

Nuclear spallation describes the process of violent disintegration of a target nucleus upon being struck by an energetic projectile. The resulting fragments can retain energies up to the projectiles energy. The spallation term in the transport equation considers both the destruction (first term), as well as creation (second term) of CRs i from heavier types j . It is assumed that spallation from type $j \rightarrow i$ occurs at a constant probability of p_{ij} in a characteristic time frame $\tau_{\text{spal.}, j}$.

- **Weak decay** $(n_i / \tau_{\text{rad.}, i} - \sum n_j d_{ij} / \tau_{\text{rad.}, j})$:

If a particle j is weakly unstable ($\tau_{\text{rad.}, i} < \infty$) there is a nonzero chance d_{ij} it decays into a daughter nuclei of some type i during propagation. The decay term reflects this and describes both decay from heavier and decay into lighter nuclei.

Insights to the physical implications of this parametrization can be gathered from a simplified example. Consider the case of a galaxy with height $2H$ and width W . It is $H \ll W$, and thus only diffusion along the $\pm z$ -direction will be examined. Considering n_0 protons located at $z = 0$ initially, and ignoring interactions with the ISM, the transport equation reduces to the first two terms, with $D = (0, 0, D_z)^T$ and $Q = n_0 \delta(z) \delta(t_0)$.

It can quickly be verified that a solution to the transport equation in this case is given by a normal distribution with mean $\mu = 0$ and standard deviation $\sigma = \sqrt{2D_z t}$. The diffusion coefficient D_z is a measure of how quickly the population spreads out (along the $\pm z$ -direction). According to [28], D_z can be parametrized via the particles energy E_p , and characteristics of the present \vec{B} -fields.

$$D_z = \frac{1}{3} \frac{E_p}{m_p c^2} \cdot \frac{|\vec{B}| \cdot \langle L_{\vec{B}} \rangle}{\sqrt{\mu_0 \rho_{\text{ISM}}}}, \quad (2.9)$$

where $\langle L_{\vec{B}} \rangle$ is the characteristic length scale of deflecting \vec{B} -fields, μ_0 and ρ_{ISM} are the magnetic vacuum permeability and density of the interstellar medium respectively. After some time t , a fraction $r_{\text{esc.}}(t)$ of particles will have a z -coordinate $|z| > H$, and

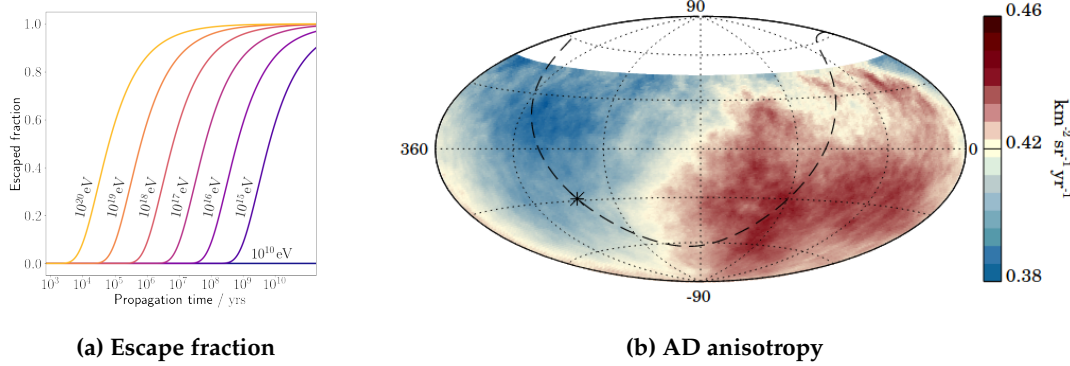


Figure 2.2: (a) $r_{\text{esc.}}(t)$ according to Equation 2.10 for protons of different energies.
(b) Dipole in the arrival direction of CRs with $E > 8$ EeV. Image copied from [27].

exit the disc consequently. In reality, this is not equivalent to the particle leaving the galaxy, as large-scale halo structures extend above and below the visible disc [29]. These halos are ignored here. $r_{\text{esc.}}(t)$ can thus be calculated according to Equation 2.10. For some selected energies, a plot of the escaping ratio over time is offered in Figure 2.2a.

$$r_{\text{esc.}}(t) := 1 - \int_{-H}^H \frac{n(z, t)}{n_0} dz \quad (2.10)$$

It can be concluded that low energy CRs do not travel outside their host galaxy within reasonable timeframes. Meanwhile UHECRs with energies exceeding $E > 10^{18}$ eV escape swiftly on ballistic trajectories and are thus likely have an extragalactic origin, not last also due to the limited energies that CR sources in the milky way can provide.

This observation is consistent with a dipole in the Arrival Direction (AD) of UHECRs observed by the Pierre Auger observatory. The dipole points roughly in the opposite direction of the galactic core, marked with an asterisk in Figure 2.2b.

2.3.2 Extragalactic propagation & GZK-Cutoff

In the last paragraph the (likely) extragalactic origin of UHECRs was discussed. Such particles must traverse millions of lightyears of extragalactic space before inducing a large air shower on earth. As the energy of these primaries increases above the Greisen-Zatsepin-Kusmin threshold (GZK), their propagation through space is thought to be severely impeded. At energies above $\approx 10^{20}$ eV the Cosmic Microwave Background (CMB) consisting of photons in the microwave range are blueshifted to energies $E_\gamma > 300$ MeV. A proton with the corresponding energy can thus absorb such CMB photons and convert to its' excited spin state, the Δ^+ -baryon. The Δ^+ -baryon decays nearly instantaneously to (for example) the ground state again, by radiating away a π^0 and losing energy in the process [30].

The mean free path of this interaction, also labelled GZK horizon is both energy- and primary-dependant. For 75 EeV protons, it is ≈ 100 Mpc [31]. Cosmic rays exceeding the GZK threshold should ergo not be observed from faraway sources, and an overall reduction in flux at these energies should be recorded [32].

Indeed, results published by the Auger collaboration (see section 2.5) are consistent with this assumption. Whether or not the GZK-supression is the main cause for this soft spectrum at the highest energies remains unclear for now, but might be answered with the ongoing AugerPrime upgrade of the Pierre Auger observatory.

2.4 Composition

The composition of CRs largely mirror the relative abundancies of elements in the universe with some noteable exceptions shown in Figure 2.3. Elements like beryllium (Be) or vanadium (V) are atypical products of supernovae and thus not as common as e.g. oxygen (O) [33, 34] in the solar system. This leads to a dip in the corresponding abundance spectrum. The same dip is not observed in CR primary abundancies. While it is a priori existant upon creation of cosmic rays, it gradually gets "filled up" via e.g. spallation processes during their propagation until an equilibrium state is reached.

This equilibrium state depends sensitively on the characteristic age of cosmic rays, i.e. the mean travel time until a particle escapes the galaxy. Measuring CR composition hence enables the estimation of this parameter. Such an analysis is conducted in [35], where it is found that the observed abundancies are consistent with a characteristic age of 1.7×10^7 yr for such high energy particles.

Contrary, hydrogen (H) and helium (He) are underrepresented (w.r.t their natural abundance in the solar system) in cosmic ray particles. This is likely due to the comparably high ionization energy of both elements, which leads to less readily available hydrogen/helium ions. Since the acceleration mechanisms discussed in section 2.2 all couple to the net charge q of a particle, unionized hydrogen and helium are not accelerated [36].

2.5 Energy spectrum

It has been discussed in section 2.2 that the expected CR flux w.r.t energy for supernova remnants is a powerlaw in the rough range of $200 \text{ MeV} < E \lesssim 100 \text{ TeV}$. Observations by various experiments extend this result to even higher energies. Their combined results are shown in Figure 2.4. However, while the general assumption of a powerlaw $\Phi(E) \propto E^\alpha$ holds over a large range of energies, kinks and other feature in the spectrum indicate that the spectral index α is not uniform, and instead a function of energy. The approximate form of $\alpha(E)$ will be discussed in the following by examining several key regions of the energy spectrum.

- **Proton knee:**

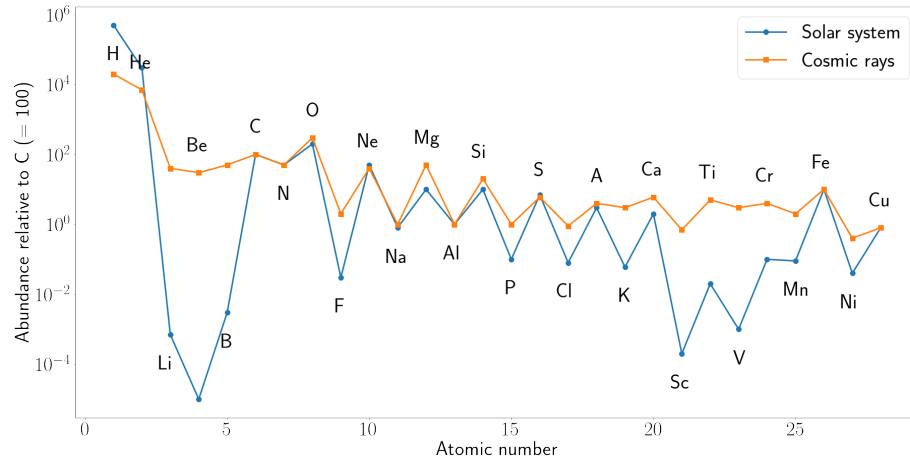


Figure 2.3: Composition expressed as abundancy relative to carbon for different sources. The ragged, alternating structure stems from an increased stability of nuclei with an even amount of protons (c.f. for example [37]). Data from [38]

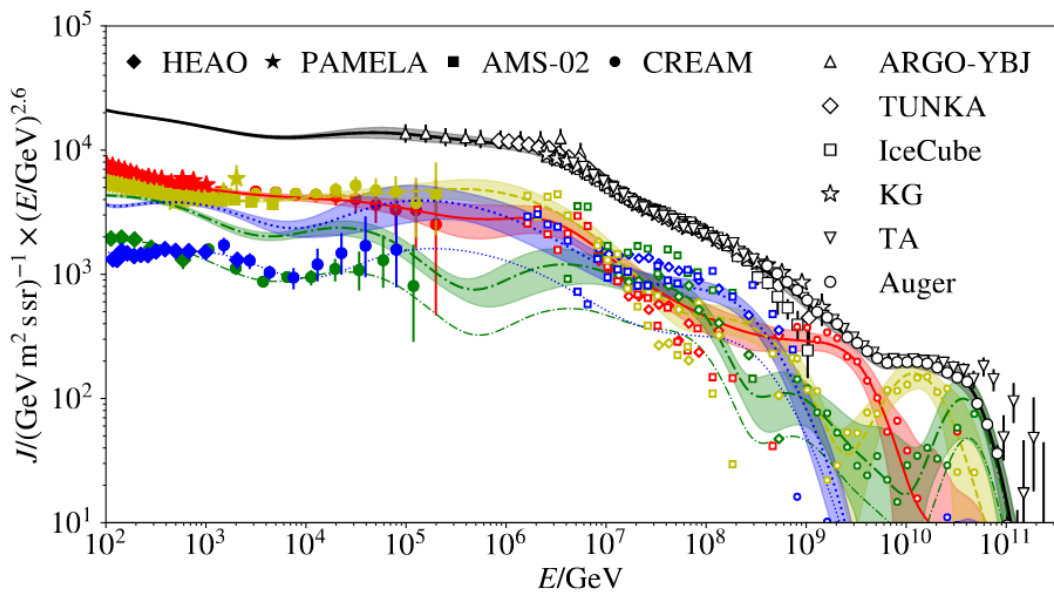


Figure 2.4: Measurements of the cosmic ray flux, multiplied by a factor $E^{2.6}$ for all types (black), and broken down by primary. Shown are protons (red), helium (yellow), oxygen (green) and iron (blue). Plot adopted from [39].

Below an energy of $\approx 1 \text{ PeV} = 10^6 \text{ GeV}$, it is $\alpha(E) \approx 2.7$, while above a spectral index of $\alpha(E) \approx 3.0$ is found [38]. This softening of the spectrum (i.e. fewer particles of higher energy) could be attributed to several effects.

- **Dark matter channel** (partially falsified)

Weakly Interactive Massive Particles (WIMPs) are a popular candidate for Dark Matter (DM), as they correctly estimate the cosmological evolution of the universe [40]. A WIMP with a sufficiently high mass could explain the kink in the energy spectrum. CRs with $E > m_{\text{WIMP}}c^2$ could in theory produce DM in deeply-inelastic scattering processes. The degree of steepening in the spectrum is a measure for how readily the process $X \rightarrow \text{WIMP} + Y$ occurs. The steeper the spectrum gets, the more particles are converted to DM, and the higher the corresponding cross sections are. Most theories involving WIMP creation can be excluded, since detectors at earthbound particle accelerators should have observed DM production at the observed steepening from 2.7 to 3.0 [41].

- **Escape during propagation**

While the analysis in subsection 2.3.1 concludes that the escape time for 10^{15} eV protons to leave their host galaxy is at least of the order 10^8 yr (compare Figure 2.2a), the calculations leading to this result are extremely simplified. If a more accurate treatment finds that particles with rigidities corresponding to the relevant energies are no longer confined by galactic magnetic fields, the kink could originate from particles leaving the milky way and not contributing to the flux observed on earth any longer.

- **Limited source energy**

A last possible explanation might lie in Equation 2.8. A prevalent acceleration mechanism for CRs below 10^{15} eV , such as shock acceleration in SNRs for example, might not be able to provide energies exceeding this threshold due to physical constraints. The spectrum above the proton knee is thus populated by CRs that originate from different acceleration mechanisms with different relations $\alpha(E)$.

- **Iron knee:**

The spectrum exhibits various similar kinks at slightly higher energies than the one of the proton knee. While it is assumed that they are ultimately caused by the same physical principles, each one corresponds to a different primary particle. Representative, the iron knee at $E \approx 10^{17} \text{ eV}$ is discussed here.

Because iron has both a higher mass and charge ($Z = 26$, $A = 56$) compared to the proton ($Z = A = 1$), different processes couple to the different nuclei with disparate strength. In particular, an iron core has a higher magnetic rigidity $R \propto \frac{A}{Z}$ than a proton of equivalent energy. This is explained by the fact that, while the iron core experiences a larger Lorentz force ($\propto Z$), the resulting acceleration ($\propto \frac{Z}{A}$) is not as strong due to a disproportionately larger mass ($\propto A$). It is thus logical

to expect differences in the creation, propagation, and shower characteristics (see section 3.3 for details) of different CR primary particles. By extension, the spectral index $\alpha(E)$ should be contrasting for each distinct particle type i , giving rise to different fluxes $\Phi(E)_i$, which is confirmed by Figure 2.4.

The ultimate cause of the different knees remains unknown currently. In the context of the ongoing AugerPrime upgrade, the Pierre Auger observatory will scan the energy spectrum at higher precision [42]. This will allow to test whether the location of the various kinks scale with A or with Z , and consequently shed light on the processes giving rise to these features.

- **Ankle:**

At an energy of roughly $\approx 1 \text{ EeV} = 10^9 \text{ GeV}$ an inflection point is found, where the spectrum hardens again from an index $\alpha(E) = 3.0$ to ≈ 2.7 . This might mark the final transition from predominantly galactic to intergalactic cosmic rays. If intergalactic CR sources such as AGNs have a harder spectrum (but lower luminosity) than galactic sources, the ankle could be well explained by a smooth transition from the latter to the former spectrum [43]. Other explanations focus on a change of the primary composition, which seems to be apparent in Figure 2.4 at the correct energy [44]. In any case, more data needs to be gathered to come to an informed conclusion on the ultimate cause.

- **Suppression:**

At energies beyond 10^{20} eV a sharp drop in the flux can be noted. This represents the tail end of the spectrum, beyond which events are so rare that cosmic ray observatories can mostly just identify upper limits with their available statistics. The cause for the drop is actively debated, and might lie in the GZK cutoff discussed in subsection 2.3.2. Another explanation might be that the tail end represents the point at which even the largest and most powerful (in terms of energy) CR sources in the universe are not able to accelerate particles any further (c.f. Figure 2.1).

3 Extensive air showers

Extensive air showers describe the particle cascades that are the result of a high-energy cosmic ray interacting with the atmosphere of the earth. While the microstate of a given air shower is inherently chaotic, macroscopic variables such as the number of particles in the cascade, its' multiplicity, allow conclusions on the primary cosmic ray.

In this chapter the various processes which give raise to the jets of energetic particles are discussed. Because hadronic primaries that carry intrinsic SU(3)-color charges are fundamentally different from leptonic ones which do not, this is done in a two-fold way. The fundamental principles giving rise to electromagnetic cascades are shown in section 3.1. Supplementary information regarding hadronic showers is listed in section 3.2. Finally, the effect of differing hadronic primaries is considered in section 3.3.

3.1 Electromagnetic showers

The dominating interaction of $E > 10 \text{ MeV}$ photons in matter is e^+e^- pair production, whereas for electrons/positrons the creation of a γ via bremsstrahlung prevails at high energies. This is shown in Figure 3.1. Consequently, an entire cascade of e^\pm and photons can emerge from a single primary particle, as realised by Heitler in [47].

Of particular interest in these showers are, apart from the primary particles energy E_0 and arrival direction (Φ, θ) , the atmospheric depth X_{\max} at which it reaches its' maximum multiplicity, as well as the Lateral Distribution Function (LDF), that parametrizes the distribution of particles along the shower axis. An important variable that influences both values is the radiation length X_0 . It represents the characteristic length at which an e^\pm loses $1 - \frac{1}{e} \approx 63\%$ of its energy. It also corresponds to the mean free path of a photon in matter up to a factor 7/9 [gupta2010calculation]. Neglecting said factor and assuming that new particles on average inherit half of the parent energy, describing the multitude of particles contained in an electromagnetic shower becomes a counting exercise in the context of the Heitler-model.

With each radiation length, the number of particles N in the shower double, while the energy per particle E_{pp} halves. After traversing an atmospheric depth of $n \cdot X_{\max}$, typically measured in units of $\frac{\text{g}}{\text{cm}^2}$, they consequently read

$$N(n) = 2^n, \quad E(n) = \frac{E_0}{2^n}. \quad (3.1)$$

After sufficient interactions, the energy of each individual particle E_{pp} will have degraded to such an extent that other processes are no longer negligible compared to

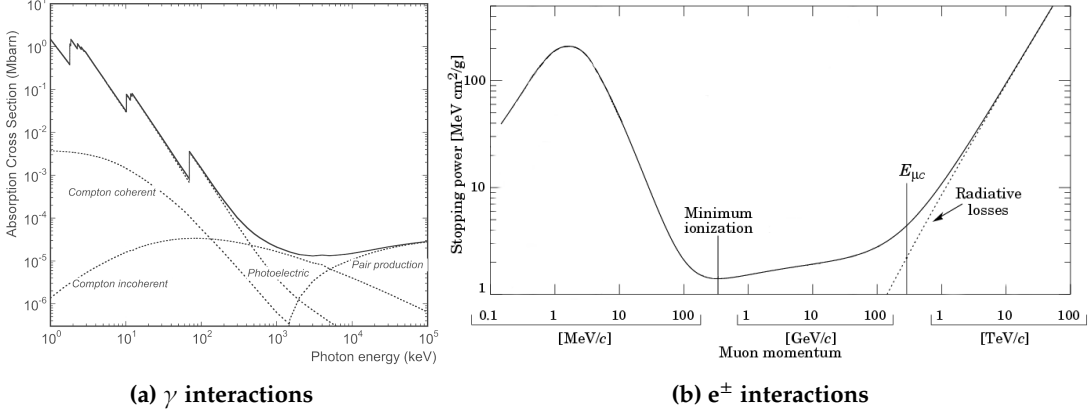


Figure 3.1: (a) Cross section for different energy loss processes of a photon in tungsten. The sudden spikes correspond to the transition energy of increasingly higher-energy electron shells. From [45]. (b) Stopping power of copper, representatively on an antimuon μ^+ , with respect to its' momentum. Plot adopted with changes from [46].

bremsstrahlung and pair production. This occurs at the critical energy $E_{c, \text{EM}}$ below which the shower rapidly stops creating new particles and dies out as a result. It follows via Equation 3.2 and 3.3 that both X_{\max} as well as N_{\max} increase with E_0 . The multiplicity arising from these assumptions alongside a stylized propagation of the thus created shower is represented in Figure 3.2.

$$\begin{aligned} E_{\text{PP}}(n_{\max}) &\stackrel{!}{=} E_c \stackrel{(3.1)}{=} \frac{E_0}{2^{n_{\max}}} \\ \Leftrightarrow n_{\max} &= \left\lfloor \log_2 \left(\frac{E_0}{E_{c, \text{EM}}} \right) \right\rfloor \\ \Rightarrow X_{\max} &= n_{\max} \cdot X_0 = \left\lfloor \log_2 \left(\frac{E_0}{E_{c, \text{EM}}} \right) \right\rfloor. \end{aligned} \quad (3.2)$$

$$\Rightarrow N_{\max} = 2^{n_{\max}} = \left\lfloor \frac{E_0}{E_{c, \text{EM}}} \right\rfloor. \quad (3.3)$$

The number of particles at a given distance from the shower axis (y-axis in Figure 3.2) is essentially random, but follows a statistical basis, the lateral distribution function. The LDF can either be derived approximately from first principles [48] or empirically, as is done in [49]. The latter arrives at a closed form approximation for the local density ρ of particles given a shower with multiplicity N at a distance r from the shower axis as

$$\rho_{\text{EM}}(N, r) = \frac{0.4 N}{r_M^2} \left(\frac{r_M}{r} \right)^{0.75} \left(\frac{r_M}{r + r_M} \right)^{3.25} \left(1 + \frac{r}{11.4 r_M} \right). \quad (3.4)$$

In Equation 3.4, the Molière radius r_M characterizes the lateral spread in multiple scattering processes. It is of order $r_M \approx 100$ m for interactions that are relevant here, and in general depends on the density of the considered material [50].

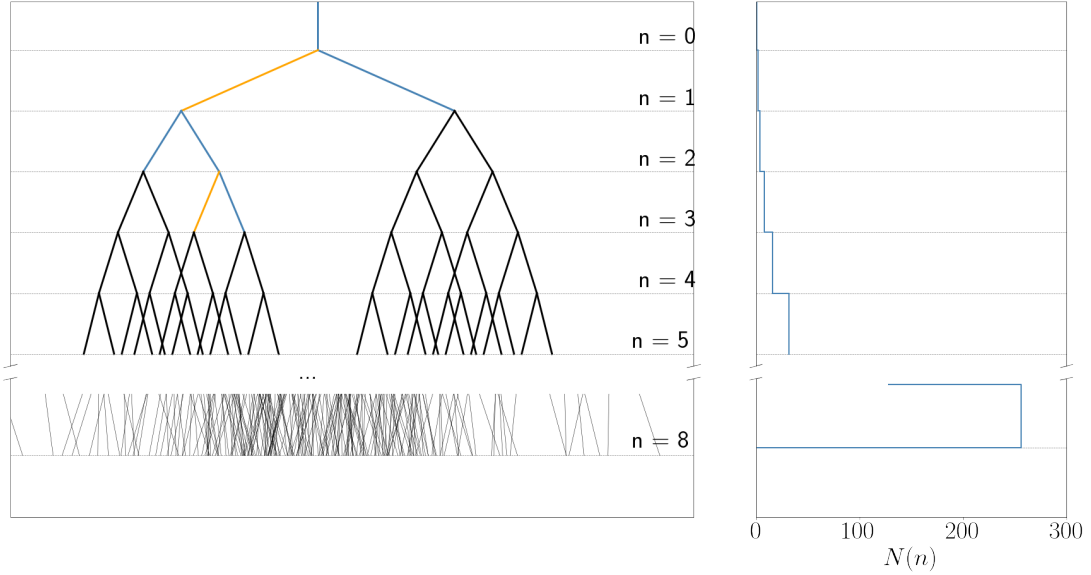


Figure 3.2: Shown on the left is the stylized propagation of an extensive air shower through the atmosphere according to the Heitler-model, quantized in units of X_0 . The energy of the primary particle is of order $2^8 \cdot E_{c,EM}$, which allows for 8 bifurcation steps, and $N_{\max} = 256$ shower particles. The multiplicity of the shower after each step is shown in the right subplot.

3.2 Hadronic showers

Hadronic primaries will readily produce color-charged secondaries, as has been shown many times in particle accelerators. In order to model the development of hadronic showers, the model discussed in Equation 3.1 thus needs to be adjusted. An example theory has been developed by Matthews in 2005. Following the reasoning in [51], after traversing an atmospheric depth corresponding to the hadronic interaction length, a proton creates on average $N_\pi \approx 15$ pions, of which two thirds are charged, and one third is uncharged. The corresponding decay channels of the light π -mesons with the largest Branching Ratios (BR) are

$$\begin{aligned}\pi^+ &\rightarrow \mu^+ + \nu_\mu & (\text{BR} \approx 0.9999, \tau = 2.6033 \times 10^{-8} \text{ s [30]}), \\ \pi^- &\rightarrow \mu^- + \bar{\nu}_\mu & (\text{BR} \approx 0.9999, \tau = 2.6033 \times 10^{-8} \text{ s [30]}), \\ \pi^0 &\rightarrow 2\gamma & (\text{BR} \approx 0.9882, \tau = 8.5 \times 10^{-17} \text{ s [30]}).\end{aligned}$$

With a mean lifetime of just attoseconds, the π^0 decay instantly before being able to continue the cascade process. In this fashion, the uncharged particles initiate a Heitler shower such as the one in section 3.1, by providing high-energy photons. It follows that every hadronic shower has an electromagnetic component. Moreover, assuming that the inherited energy from the parent particle is roughly uniformly distributed among its' children, one third of the remaining energy in the hadronic component is lost to the electromagnetic component per hadronic interaction length.

Meanwhile, the charged pions repeat the procedure of creating secondary mesons, kicking off the hadronic component of the shower in the process.

Similar to the reasoning in section 3.1, a primary of given energy initiates a shower of a specific multiplicity N_{\max} . This is reached after n_{\max} steps, where the energy per particle $E_{\text{PP}}(n_{\max})$ is below the critical energy $E_{c,\text{had}}$ at which the mesons ionize rather than continue the cascade. After this last step, the charged pions eventually decay into muons and neutrinos. The shower characteristics are thus given by

$$N_{\text{had}}(n) = \left(\frac{2N_\pi}{3}\right)^n, \quad E_{\text{PP}}(n) = \frac{E_0}{N_\pi^n}, \quad n_{\max} = \left\lfloor \log_N \left(\frac{E_0}{E_{c,\text{had}}}\right) \right\rfloor, \quad (3.5)$$

wheras the maximum multiplicity (ignoring neutrinos) in the shower is calculated as

$$N_{\max,1} = \underbrace{\frac{3}{2} \left(\frac{2}{3} N_\pi\right)^{n_{\max}}}_{\text{Muon component}} + \underbrace{\sum_{k=1}^{n_{\max}-1} \frac{N(k)}{3} \cdot \left\lfloor \frac{E_{\text{PP}}(k)}{E_{c,\text{EM}}} \right\rfloor}_{\text{EM component}}. \quad (3.6)$$

The muons stemming from pion decay follow a different LDF than the electromagnetic component. Again following the analysis in [49], the muonic LDF can be recovered as

$$\rho_\mu(N, t) = 18 \left(\frac{N}{10^6 \cdot r}\right)^{\frac{3}{4}} \cdot \left(1 + \frac{r}{320}\right)^{-\frac{5}{2}}. \quad (3.7)$$

While the above Equation 3.7 drops off slower $O(r^{-\frac{3}{2}})$ compared to the electromagnetic component ($O(r^{-3})$), the immediate vicinity of the shower axis contains mostly photons and leptons from the EM subshower. Further out, the muonic component takes over. This is visualized in Figure 3.3. Due to this reason, and the fact that muons can carry considerable amounts of energy faraway from the shower axis, the muonic footprint of a shower often appears much more "patchy" compared to the EM portion. This knowledge is especially useful when distinguishing between hadron- and photon-induced air showers (compare [52]).

3.3 Composite primaries

As is evident from the discussion in chapter 2, not only single protons (which are strictly speaking also composite) or elementary particles like photons, electrons, etc. appear in the cosmic ray spectrum. In theory, any somewhat stable particle is a possible primary. The consequence of different primaries on resulting shower characteristics is subtle, but large enough such that it can be used for identification purposes.

Assuming the constituents in a CR nucleus all coherently interact with an air molecule, one arrives at the superposition principle for extensive air showers. It states that for a

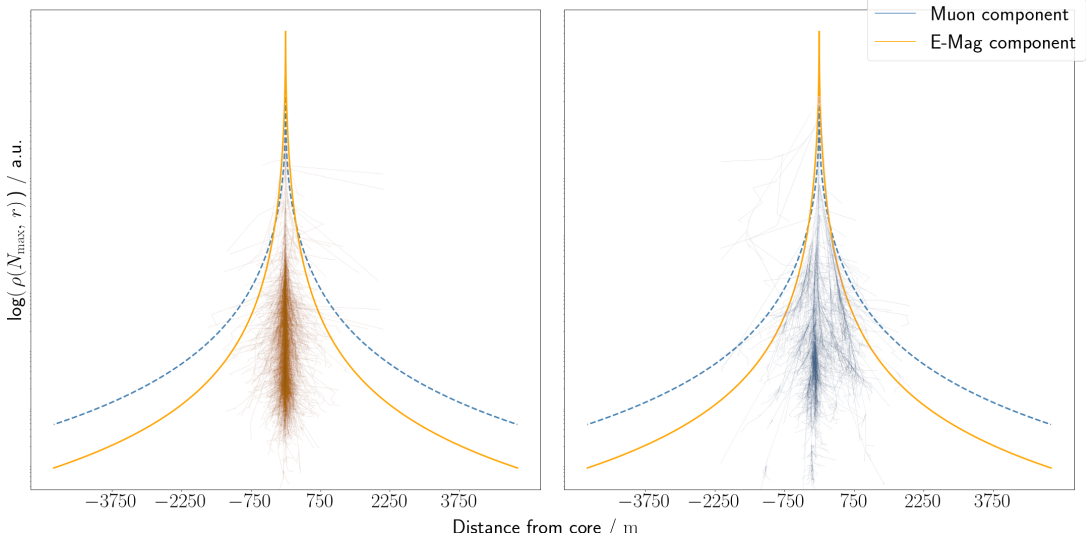


Figure 3.3: The lateral distribution function for the muonic (steelblue) and electromagnetic (orange) component of a vertical, 100 GeV proton shower at roughly sea level ($r_M = 100$ m). The inset plots represent the xz-projection of the color-coded shower component. Both component images adopted with changes from [53].

composite primary with $A = N + Z$ neutrons and protons, each constituent particle will initiate a subshower with initial energy of $E'_0 = E_0 / A$, where E_0 is the initial energy of the composite particle. For this scenario, N_{\max} and n_{\max} are known from the preceding sections. It follows that air showers from heavier primaries occur at higher altitudes (lower atmospheric depth X) and with higher particle counts.

$$N_{\max, A} = A \cdot N_{\max}, \quad n_{\max, A} = \left\lfloor \log_N \left(\frac{E_0}{E_{c, \text{had}}} \right) - \log_N A \right\rfloor, \quad (3.8)$$

where $N_{\max, A}$, $n_{\max, A}$ refer to the resulting extensive air shower characteristics that are induced by a particle with mass number A . On top of this, because more massive particles initiate more subshowers of comparably lower primary energy, and thus have lower n_{\max} , less energy is transferred from the hadronic to the electromagnetic shower component. This results in differing fractions of muonic to electromagnetic signal in the shower footprint.

3.4 Comments on validity

The Heitler model and Heitler-Matthews model discussed in section 3.1 and section 3.2 respectively make only very rudimentary assumptions on the underlying physics of particle cascades. Nevertheless, the equations recovered from these assumptions are already a close approximation of real world processes up to X_{\max} .

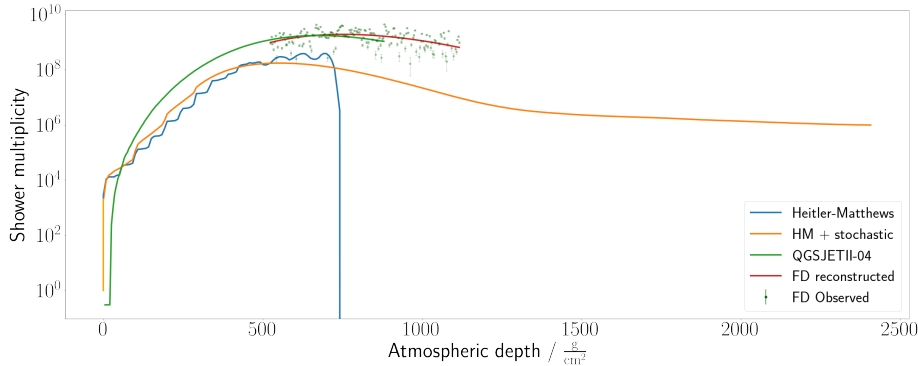


Figure 3.4: Comparison of the number of charged particles for different physics models to reconstructed observations from a 3 EeV proton shower. Shown in steelblue and orange is the Heitler-Matthews model as described in section 3.2, and extended with a stochastic component. An example of a more in-depth simulation in red, and observed shower multiplicities in green.

Of course, adding a stochastic component to the above assumptions (c.f. [54]) improves predictions. But even full-fledged Monte-Carlo simulation software frameworks like GEANT4 [55] or CORSIKA [56] show discrepancies between observed and predicted shower development when analysed in depth. This is shown in Figure 3.4.

While shower-to-shower fluctuations can explain discrepancies to a degree, there also exist systematic differences between the simulated and observed extensive air showers. These are largely owed to imprecise knowledge of the underlying physical processes. For example, hadronic interaction models (e.g. QGSJETII-04) rely on extrapolation of measured cross sections in the GeV-TeV scales to the relevant CR energies [57]. While this is not an unfair assumption given the scale invariance of deep inelastic scattering [58], it is clear, that the approach cannot accurately encompass all effects that may take place at the high energies present in atmospheric particle cascades.

In conclusion, the particle cascades evolving from relativistic CRs impinging on earth are still not fully understood. Several simulation frameworks have been developed, which each have their own shortcomings. It is therefore important to compare not only results from simulations using one framework to observations, but also different simulations with each other.

3.5 Detection methods

3.5.1 Cherenkov light

When a charged particle exceeds the phase velocity of light in a medium with refractive index n , the optical equivalent of a sonic boom occurs. Photons travel in a shockwave along an angle $\theta = \arccos(n^{-1}\beta^{-1})$ relative to the trajectory of the particle while $\beta \geq \frac{c}{n}$. This process is well understood and can be used to detect high energy cosmic rays.

Imaging Air Cherenkov Telescope

The refractive index of air ranges from 1 in the near vacuum of the upper atmosphere to $\approx 1 + 2.9 \cdot 10^{-4}$ at sea level [59]. This implies that particles with a Lorentz factor $\gamma \gtrsim 41.5$ emit Cherenkov light, which is satisfied for e.g. muons and protons in the low GeV ranges and above.

It can therefore be expected that extensive air showers, which contain high energy charged particles, produce considerable amounts of Cherenkov light when propagating through the atmosphere. This light, and by extension the air shower can be detected with Imaging Air Cherenkov Telescopes (IACTs). Ground based experiments such as VERITAS [60] or H.E.S.S [61] detect gamma-rays using this technique.

Water Cherenkov Detector

The lightspeed in water is roughly 33% slower than in vacuum. Cherenkov radiation in water therefore occurs more easily than in air. Using this reasoning, a water tank equipped with means of detecting the emitted Cherenkov light, via e.g. PhotoMultiplier Tubes (PMTs), should be able to measure traces of an air shower.

Indeed, this exact measurement principle of a Water Cherenkov Detector (WCD) was and is adopted in a variety of cosmic ray observatories such as the Pierre Auger observatory [62], HAWC [63], or Kamiokande [64], for example.

3.5.2 Fluorescence

Ionization losses have been ignored in the discussion of the formation of extensive air showers. This is of course not completely accurate. During the development of an extensive air shower, particles excite, or even ionize the permeated medium. Consequently, spontaneous emission of photons due to recombination, or transition back to a ground state can be observed. The amount of fluorescence light produced in this way is a gauge for the number of particles present in the shower at a given moment.

In Air

The predominant element in air is nitrogen (78%), whose transitions lay in the UV-band [65]. After a nitrogen molecule is excited by a passing shower particle, a photon with wavelength $300 \text{ nm} \leq \lambda \leq 430 \text{ nm}$ is emitted isotropically due to relaxation. The low attenuation of ultraviolet radiation in air allows the fluorescence light to travel large distances before being absorbed [66]. This enables cameras like EUSO-TA [67] or the Fluorescence Detector (FD) of the Pierre Auger observatory (see [65] and section 4.1) to observe traces of extensive air showers from faraway during their development.

However, because of the low light yield of just 5 photons/MeV [68], the detectors must operate in low UV-noise conditions, which places an upper limit on their duty cycle.

In Scintillators

Conventional plastic scintillators have a light yield, that is 1000–10000 times higher than that of air [69]. Such scintillators therefore pose an effective way of measuring a shower footprint on the ground. The Pierre Auger Surface Detector (SD) is equipped with scintillators during the ongoing AugerPrime upgrade. Predecessors like KASCADE [70] have been using scintillation light to detect cosmic rays as well.

3.5.3 Radio Emission

Relativistic charged particles in the cascade are subject to deflections due to the geomagnetic field. This deflection is largest for e^\pm due to their comparably tiny masses. Albeit the deflection of a typical electron in the shower is minuscule and the subsequent emission of Bremsstrahlung tiny, coherence effects along the entire shower front can greatly amplify the electric field strengths obtained from this effect [71]. This gives rise to radio signals emitted by the extensive air shower, which can in principle be detected via antennas.

One challenge in constructing an efficient CR radio detector is the requirement for a radio-quiet environment, where a large enough Signal-to-Noise-Ratio (SNR) permits analysis of measured data. This is the case for the AERA component of the Pierre Auger observatory, which has been in operation since 2010 [72]. Its results have in part lead the proposal of a vast radio array, GRAND [73], which will have an enormous exposure to CR showers, if built.

4 The Pierre Auger Observatory

Located on the argentinian high-plains of Pampa Amarilla, the Pierre Auger observatory is a hybrid detector designed to detect and study cosmic rays of the highest energies. With an effective area of 3000 km^2 it is by far the largest experiment of its kind [74].

Altough first proposed in 1992, it took 18 years until the idea of a large scale experiment to detect cosmic rays matured and construction of the first prototype started near Mendoza [75]. Some further 20 years later, the Pierre Auger collaboration has published over 110 papers [76] and continues to advance research in astroparticle physics.

It does this via a hybrid approach, combining measurements of a **Surface Detector** (SD) as well as a **Flourescence Detector** (FD). Additional machinery, such as the **eXtreme** (XLF) and **Central Laser Facility** (CLF), is installed to monitor atmospheric variables. This improves the overall systematic accuracy of predictions made by the experiment. An overview of the site can be seen in Figure 4.1. Data measured by the FD, SD and the atmospheric monitors is sent to a **Central Data Acquisition System** (CDAS) located in the nearby town of Malargüe.

This chapter offers a brief look into the measurement principle and setup of the observatory. Information regarding the fluorescence detector can be found in section 4.1. The SD is described in section 4.2. A more in depth read on detector specifications and design choices is represented by the Pierre Auger observatory design report [74], where a lot of information stated in this chapter is conglomerated from. Notes on the event reconstruction are listed in section 4.3 and summarized from [77] and [65].

4.1 Fluorescence Detector (FD)

The FD consists of a total of 27 fluorescence telescopes (eyes) at 4 different sites. Each eye monitors a $30^\circ \times 30^\circ$ window of the sky at a resolution of $\approx 0.5 \frac{\text{px}}{\text{deg}^2}$. This results in an effective FOV of roughly $180^\circ \times 30^\circ$ per FD station, with an exception of Coihueco, where three additional telescopes - HEAT (High Elevation Auger Telescope) - are installed to enable monitoring of higher zenith angles ($30^\circ \leq \theta \leq 60^\circ$) and increase sensitivity for showers of lower energies (compare chapter 2). A schematic of the setup of each eye is given in Figure 4.2a.

The individual telescopes consist of 3.6 m by 3.6 m, convex mirrors. They reflect incoming light onto a set of 440 photomultipliers (PMTs), each corresponding to one pixel in the resulting image seen by an eye. Since the setup needs to be extremely sensitive to UV light in order to detect flourescence caused by extensive air showers, its operation is limited to the relatively noise free moonless astronomical nights (Sun

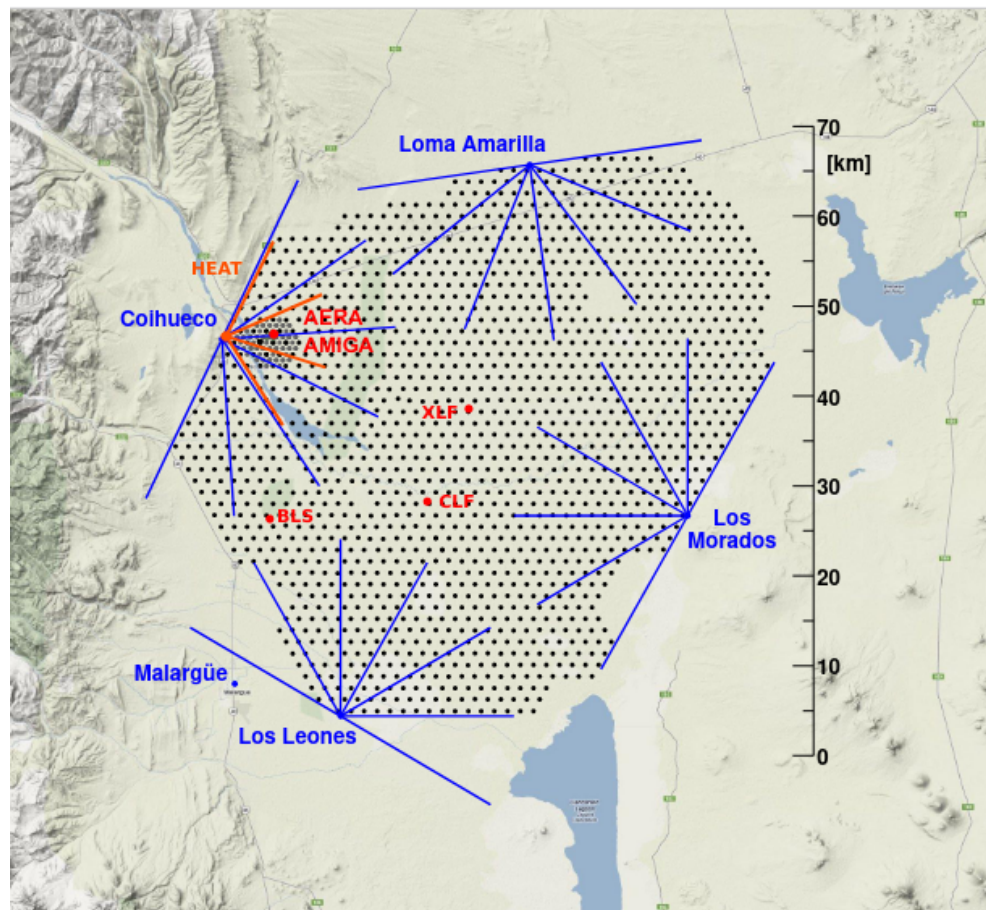


Figure 4.1: Overview of the Pierre Auger observatory. The four different FD sites (respective FOV shown with blue lines) sit at the edge of the detector area and monitor the night sky above the SD array consisting of 1600 water tanks (black dots). A denser spacing of stations near Coihueco is equipped with additional electronics such as e.g. radio antennas (AERA) and muon detectors (AMIGA). Image taken from [78]

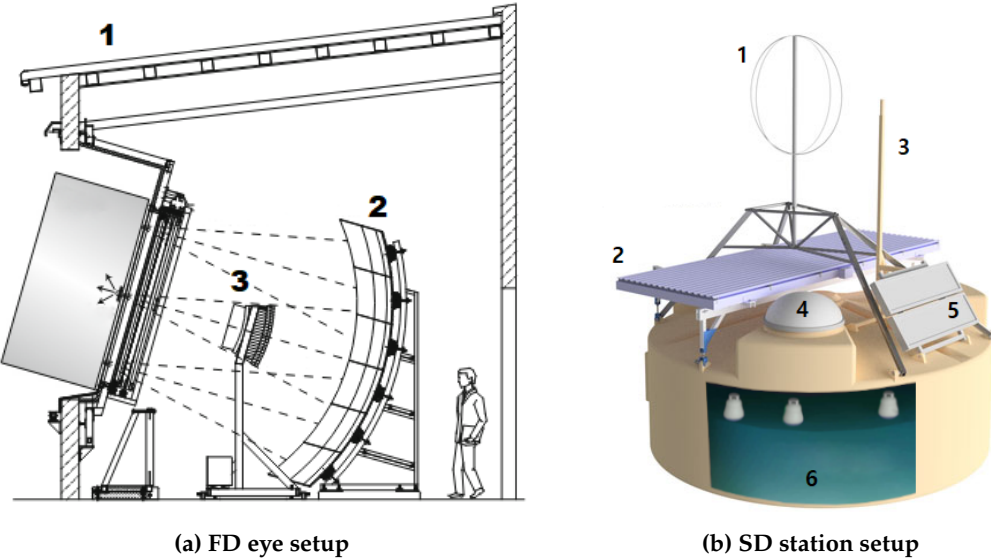


Figure 4.2: (a) Schematic view of an FD eye with housing (1), main mirror (2) and camera (3). Image taken from [65] (b) Setup of an SD WCD with radio antenna (1), SSD (2), communication and GPS antenna (3), electronics box (4), solar panels (5) and the WCD (6). Image adopted with changes from [79] and [80]

$\angle \text{Horizon} \lesssim -18^\circ$). When the FD is operational, this allows the observation of the longitudinal propagation of a shower instead of just its' footprint (as seen by the SD).

4.2 Surface Detector (SD)

The SD consists of 1600 individually operating stations, spaced apart on a hexagonal grid with a standard 1.5 km spacing. Each station is made up of a main tank filled with 12 000 L of purified water and reflective inner walls, a solar panel and batteries for power management, as well as an antenna for communication. Within each tank three PMTs detect Cherenkov light originating from shower particles, these are together with the tank referred to as **Water Cherenkov Detectors** (WCDs). With the (at the time of this work) ongoing AugerPrime upgrade, each station is additionally equipped with a **sPMT**, **Surface Scintillator Detector** (SSD), and radio antenna atop the tank. This allows for the recording of stronger signals, finer separation of electromagnetic and muonic shower component and detection of highly inclined air showers respectively [81, 82]. Figure 4.2b shows a schematic blueprint of each SD station.

4.2.1 Data acquisition (DAQ)

Onboard electronics, the **Upgraded Unified Board** (UUB), or more precisely six 10-bit **Flash Analog-to-Digital-Converters** (FADCs) read out measurement data from the PMTs at a sampling rate of 120 MHz (≈ 8.33 ns binning) [83]. This is done in a two-fold

way. Three FADCs digitize the PMTs dynode voltage, resulting in the **High Gain** (HG) output. Three FADCs monitor the anode voltage to form the **Low Gain** (LG) output, which can be analyzed if the HG output exceeds a value of 2^{10} ADC counts and becomes saturated. This effectively enables the measurement of both large ($\geq O(10^3)$) particles hitting the tank) as well as small shower signals ($O(1)$ particle hitting the tank) with sufficient accuracy [77]. Once an FADC bin has been recorded and checked for possible triggers (c.f. chapter 7) via **Field Programmable Gate Arrays** (FPGAs) it is written to a ring buffer. If a trigger is issued, the corresponding chunk in the ring buffer ($\approx 4.992 \mu\text{s}$ (599 bins) before and $12.07 \mu\text{s}$ (1448 bins) after a trigger, 2047 + 1 bins total), the measured trace, can be analyzed in order to calibrate a station in the array (subsection 4.2.3, subsection 4.2.2) or processed by a higher-level CPU for event reconstruction purposes (see section 4.3).

While each station is equipped with the same electronics and runs the same analysis software, variables like the position in the field, station age or slight changes in the manufacturing/installation process cause different stations to age differently. Over the lifetime of the array such differences can sum into potentially drastic discrepancies in gathered data. Put simply, an extensive air shower will look different both to different WCDs at the same time as well as the same WCD at different times. To account for this, measurements are standardized across all stations. ADC counts are related to a **Vertical Equivalent of through-going Muons** (VEM) that would result in the same signal strength. In this fashion, the maximum response that is generated by a PMT from one vertically through-going muon is defined as 1 VEM_{Peak}. The total deposited charge (equivalent to the integral of the response) is defined as 1 VEM_{Ch.}. The conversion factor between ADC counts and VEM_{Peak} and VEM_{Ch.} (referred to as I_{VEM} and Q_{VEM} respectively) is estimated from data and continuously updated separately for each station. Note that due to the limited computational resources of the WCD, as well as constraints on the amount of data that can be transmitted per station in the SD array ($1200 \frac{\text{bit}}{\text{s}}$, [84]), a simplified, rate-based approach is implemented for autonomous calibration in the field (Online calibration), this stands in contrast to the more physics-driven histogram method used during event reconstruction via the official Auger reconstruction and simulation framework, Offline [85]. In any case, both algorithms are listed in the following subsections and discussed in more detail in the referenced literature.

4.2.2 Offline calibration

Baseline estimation

In order to estimate I_{VEM} and Q_{VEM} of a WCD tank first the baseline - the average response in the absence of any signals - of each PMT needs to be determined. All further analysis will then be based on the baseline-subtracted PMT data.

For event reconstruction, a first baseline estimate of a WCD PMT is predicted by examining the beginning and end of a 2048 bin ($17.06 \mu\text{s}$) long trace. The mode m as well as standard deviation σ of the first (last) 300 bins is calculated. All bins larger or

smaller than $m \pm 2\sigma$ are truncated and removed from the trace window. The value of m , σ is consequently updated and the procedure repeated until a convergence is reached and no further cut is necessary. The best estimate B_{front} (B_{end}) for the front (end) of the trace at this point is given by the mean value of all remaining bins. Its statistic uncertainty $\sigma_{B_{\text{front}}}$ ($\sigma_{B_{\text{end}}}$) is given by the standard deviation of the remaining bins [86]. The baseline between the flat front and end estimate is then interpolated based on the difference

$$\Delta B = B_{\text{end}} - B_{\text{front}}. \quad (4.1)$$

- **Rejection of anomalous upward fluctuations** $\frac{\Delta B}{\sigma_{\Delta B}} \geq +10$:

B_{end} being higher than B_{front} often indicates errors in the electronic readout or defect components in the measurement chain. There exists no physical reason why the end baseline should be (significantly) higher than the front. Consequently, traces where this is the case are ignored during event reconstruction.

- **Constant approximation for small upward fluctuations** $+5 > \frac{\Delta B}{\sigma_{\Delta B}} \geq 0$:

Small fluctuations of the baseline are expected and the norm. If these fluctuations are positive ($B_{\text{end}} > B_{\text{front}}$) the method of calculating the mode, truncating outliers and repeating both steps is applied to the entire length of the signal, resulting in a constant baseline estimate B across the trace.

- **Step-function approximation for small downward fluctuations** $0 > \frac{\Delta B}{\sigma_{\Delta B}} \geq -1$:

Unlike positive fluctuations, negative fluctuations ($B_{\text{end}} < B_{\text{front}}$) can have a physical significance. Due to the undershoot of PMTs after detecting a signal in the WCD (compare [[glietta2008recovery](#)]), the baseline estimate decreasing towards the end of the trace often indicates the presence of shower particles within the tank. For this reason, downward fluctuations are handled differently from upward ones. If the fluctuations are sufficiently small, the baseline across the trace is estimated as a simple step-function; The trace is separated into two parts along its' maximum ADC value. The front part (i.e. before the max. value) has the baseline B_{front} , while the rear part is estimated by B_{end} . An example of this is shown in Figure 4.3a.

- **Charge-linear approximation for large undershoots** $-1 \geq \frac{\Delta B}{\sigma_{\Delta B}}$:

For larger undershoots, the baseline is estimated bin by bin based on the deposited charge in the detector. Starting with a value of B_{front} for the bins 1-300, the remaining baseline is first linearly interpolated according to Equation 4.2,

$$b_i = B_{\text{front}} - \Delta B \cdot \frac{i - 300}{1448}, \quad 300 \geq i \geq 2048, \quad (4.2)$$

where the magic numbers 300 and 1448 refer to the last bin of the front baseline estimate and the length of the interpolated baseline respectively. From this, the deposited charge q_i up to bin i can be calculated as per Equation 4.3.

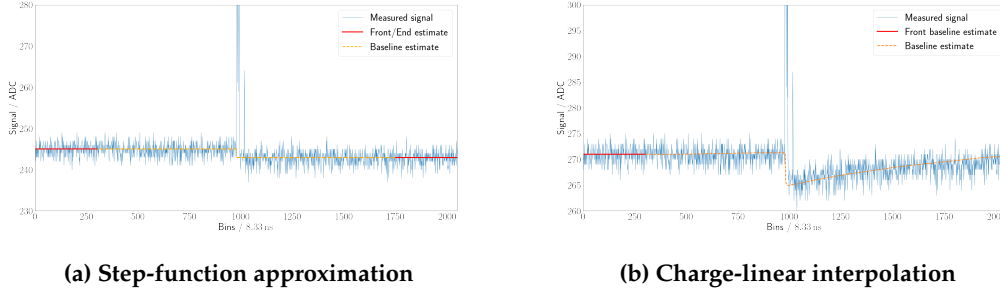


Figure 4.3: (a) A simple step function is sufficient to accurately model a PMTs' noise level at small downward fluctuations. (b) For larger discrepancies the more involved charge-linear interpolation is used. Note that the signal undershoot is exaggerated for visualization purposes in both examples.

$$q_i = \sum_{k=0}^i (T_k - b_k) \exp\left(-\frac{8.33 \text{ ns}}{\tau} \cdot (i - k)\right) \quad (4.3)$$

In Equation 4.3, T_k refers to the numerical value of bin k . Note that an exponential falloff term has to be added to account for the decay in signal undershoot with a decay time of $\tau = 45 \mu\text{s}$. The value of τ is determined in [87]. Assuming the magnitude of the signal undershoot is directly proportional to the deposited charge q , a correction of the baseline thus becomes

$$b_i = B_{\text{front}} + \frac{q_i}{q_{1898}} \cdot \Delta B. \quad (4.4)$$

The parametrization in Equation 4.4 is chosen such that the charge-interpolated baseline at bin 1898 (the center position in the last 300 bins) is exactly equal to the rear baseline estimate B_{end} . The prediction can be made more accurate by repeating the above steps, each time recalculating q_i and readjusting the baseline b_i in the process. Figure 4.3b shows an example baseline estimate after three such iterations. In general, it converges to a robust estimate within five repetitions [87].

Estimation of I_{VEM} and Q_{VEM}

The conversion factor between ADC counts and VEM_{Peak} , VEM_{Ch} , are built from distributions of traces that satisfy the muon trigger, which scans incoming ADC bins for a value exceeding the muon threshold $t_\mu = b + 30 \text{ ADC}$, 30 ADC above baseline, for any of the three WCD PMTs. If this requirement is met, 69 bins (19 before, trigger bin, 49 after) are written to the muon buffer, a FIFO (first-in-first-out) type memory storage, that is subsequently filled with low-energy events, which (in general) didn't satisfy any other trigger but still contain useful information [84].

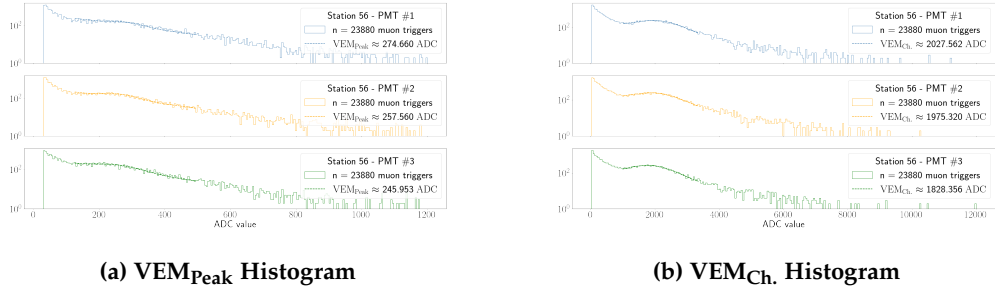


Figure 4.4: (a) The maximum value of each muon trace is histogrammed in order to gain information about the current value of I_{VEM} of a station. (b) The conversion factor from recorded ADC values to Q_{VEM} is given from the histogrammed sum of each muon trace.

By histogramming the maximum value (sum) of each trace, the plot shown in Figure 4.4a (Figure 4.4b) can be obtained. It becomes apparent that the number of events per bin largely follows a power law with negative spectral index. This is expected considering the discussion in chapter 2. Noteable are characteristic deviations from this powerlaw, as these contain information about I_{VEM} and Q_{VEM} :

- Low energy events from e.g. e^- , e^+ that deposit their entire energy in the tank give rise to a surplus of events at lower ADC values.
- A characteristic (muon) hump appears in the bins 20–70. This surplus is caused by omni-directional muons impinging onto the detector. Since the energy deposited by such muons is roughly constant, the center of the muon hump serves as an estimate of I_{VEM} (Q_{VEM}).
- (Not depicted in Figure 4.6) In similar plots from related works (c.f. [84, 88]) a drastic increase in bin occupations towards the tail end of the histograms can be observed. This is attributed to an increased bin size from 1500 ADC counts onwards, which reduces the amount of data per station sent to CDAS. In the example plots referenced here, a constant binning is chosen instead. This difference is mentioned here to avoid possible confusion.

In this fashion, the average response of the WCD to a through-going muon can be estimated by e.g. fitting a gaussian distribution to the muon hump. However, there exists a systematic difference between the response to a vertical or an omni-directional muon. Consequently, correctional factors need to be applied to the analysis results. These have been determined in previous experiments [89]. Finally, one arrives at an estimate for the conversion factor between ADC counts and VEM_{Peak} , $\text{VEM}_{\text{Ch.}}$.

4.2.3 Online calibration

Baseline estimation

Each SD station has an autonomous estimate of its' three WCD PMT baselines. They are defined simply as the mean of all first bins for each trace contained in the respective muon buffers (see subsubsection 4.2.3). This baseline estimate is used to set the thresholds of the hardware triggers discussed in chapter 7.

Estimation of I_{VEM} and Q_{VEM}

Due to the limited computational resources in each station, the determination of I_{VEM} and Q_{VEM} at station-level is fairly naive. Nevertheless, the σ - δ -method shown here has proven to be incredibly robust over the lifetime of the SD array [74].

In the beginning, the to-be-estimated value $I_{\text{Peak}}^{\text{est.}}$ ($Q_{\text{Peak}}^{\text{est.}}$) is set to the same, predefined value for all PMTs. A simple single-bin calibration trigger requiring all available WCD PMTs to be above a threshold of $t_{70} = 1.75 I_{\text{Peak}}^{\text{est.}}$ above baseline plus a given PMT exceeding $2.5 I_{\text{Peak}}^{\text{est.}}$ is used to determine a calibration trigger rate. If for some reason not all three WCD PMTs are functional, the thresholds are altered according to Table 4.1. What follows is an iterative procedure to approximate I_{VEM} (Q_{VEM}):

1. Calculate the trigger rate $r_{\text{cal.}}$ of the calibration trigger over a time $t_{\text{cal.}} = 5 \text{ s}$.
2. Adjust $I_{\text{Peak}}^{\text{est.}}$ ($Q_{\text{Peak}}^{\text{est.}}$) by $\pm\delta$ if $\pm(r_{\text{cal.}} - 70 \text{ Hz}) \geq 2 \text{ Hz}$, with $\delta = 1 \text{ ADC}$ initially.
3. If $t_{\text{cal.}} < 60 \text{ s}$ increase $t_{\text{cal.}}$ by 5 s . If $\delta > 0.1 \text{ ADC}$ decrease δ by 0.1 ADC .
4. While $t_{\text{cal.}} < 60 \text{ s}$ jump to step 1, else return $I_{\text{Peak}}^{\text{est.}}$ ($Q_{\text{Peak}}^{\text{est.}}$).

Table 4.1

n_{PMT}	t_{70}
1	2.85
2	2.00
3	1.75

4.3 Event Reconstruction

If an event has been detected (subsection 4.3.1) it is reconstructed at CDAS level, where information from all relevant detectors is conglomerated. From the observed shower footprint in the SD array as well as the (if available) longitudinal profile measured by the FD stations follows an estimate on arrival direction (subsection 4.3.3), energy

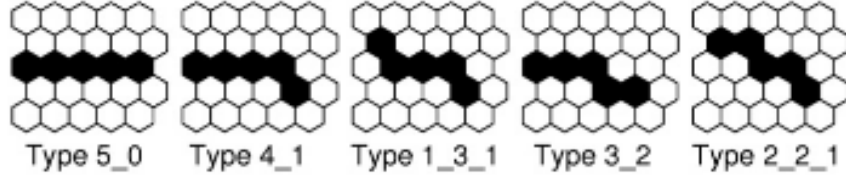


Figure 4.5: Fundamental shape of tracks considered straight. Image from [65].

(subsection 4.3.4) and primary particle (subsection 4.3.5). As the work presented in this thesis solely deals with the surface detector of the Auger observatory, this section focuses heavily on the SD reconstruction. Addendums towards FD reconstruction are given where needed.

4.3.1 Trigger procedure

The flux of cosmic rays especially at the highest energies is barely of the order of $1 \text{ km}^{-2} \text{ yr}^{-1}$ [19]. Consequently, most signals observed by the Auger observatory stem from low-energy cosmic muons and not extensive air showers. This is reflected in the hierarchical structure of the triggers, which effectively reject such events. The overall event detection is split up into three tiers, T1, T2 and T3, where T3 implies the detection of an extensive air shower by either the FD or the SD (or both).

T1 trigger

T1 level triggers are implemented at the lowest possible level. This means each FD eye or each SD station raises T1 triggers autonomously. They serve as a first indicator on whether or not a signal of any kind is present. For the most part, this is realised by checking for elevated signal strengths, i.e. for hot pixels in a FD telescopes image or PMT outputs of an SD station that are significantly above baseline. The respective trigger thresholds are calibrated such that the nominal trigger rate during operation is roughly 100 Hz [65, 77].

T2 trigger

T2 level triggers occur at the same location as T1-type triggers. They are different in their more stringent conditions on the signal size or shape. This for example entails track shape identification for the FD telescopes, where straight tracks (see Figure 4.5) of hot pixels are identified. If the resulting pixel track passes an additional quality cut that rejects e.g. lightning signals, the T2 is directly promoted to a T3 trigger (= Event). For the SD, an exact discussion of T2 triggers is given in ???. A single tank on average records T2-type events at a rate of 20 Hz and forwards this information to the CDAS along with a timestamp. There, incoming information of all tanks is scanned for spatial and temporal correlations, which indicate the presence of an extensive air shower.

T3 trigger

T3 type triggers, or event type triggers are (with the exception of FD events, which have been discussed above) built from distributions of at least three SD stations next to each other that recorded a T2 trigger in close temporal succession. Upon the detection of such a pattern a readout command is issued to all nearby stations. Their recorded FADC traces as well as calibration information are forwarded to CDAS if the station observed a T1/T2 event within an appropriate timespan of order $O(\mu\text{s})$ before or after the T3 pattern occurrence. Such a modus operandi enables an accurate reconstruction of the shower footprint by including stations that did not participate in the initial T3 trigger. This extends to FD issued T3 triggers, where potential information from SD stations in the vicinity of the FD-reconstructed shower core position is requested.

4.3.2 Core position

All reconstruction algorithms presented in the following subsections rely in one form or the other on an accurate determination of where the shower was recorded above the observatory. Hence the center of the shower footprint, the shower core, must be estimated at the beginning of the analysis chain.

Without any prior knowledge, a first guess as to where the shower core is located can be made by calculating the barycenter of all participating stations. In this fashion, a weighted mean of all station locations is constructed with weights equal to the square root of the corresponding signal strength [77].

The presented approach fails if only parts of the shower are contained within the SD event. This occurs especially at the edges of the SD array, or in the vicinity of faulty WCDs. A fiducial trigger, NT5, is employed to mitigate this problem. NT5 requires at least N active stations around the SD detector that recorded the largest signal [90].

4.3.3 Arrival direction

The shower footprint measured by the SD (example given in Figure 4.6a) corresponds to the projection of the shower plane onto the detector plane, i.e. the ground. It can be assumed that the shower plane has a fixed (hyperbolic [91]) shape and propagates at the speed of light along the primary particles trajectory. With this knowledge, estimating the arrival direction becomes a task of minimizing the difference between measured and expected arrival times given by an example shower axis anchored at the reconstructed shower core. The axis for which the summed differences is minimal corresponds to the most likely arrival direction of the primary particle.

Naturally, the expected variance on the reconstructed ϕ and θ diminishes the more stations participate in the combined fit. The angular resolution thus decreases for larger energies of the primary particle. This can be seen in Figure 4.6b. In any case, the angular resolution even at smaller energies is better than 2.2° . For hybrid events,

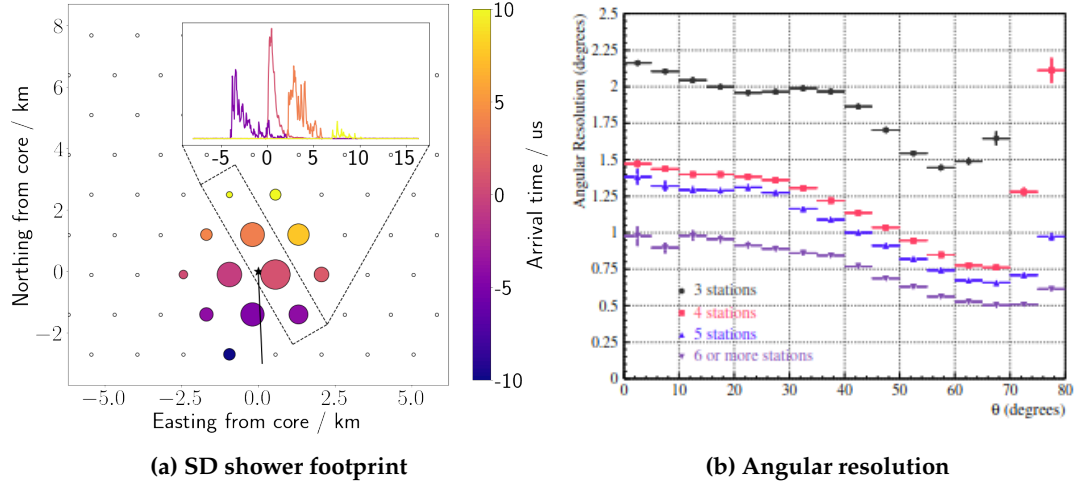


Figure 4.6: (a) An example shower footprint recorded by the individual SD tanks (circles). The measured signal strength and arrival time is encoded in the size and color for each station. Tanks that haven't recorded any signal are shown colorless. For a subset of stations the respective VEM trace and consequently the propagation of the signal in the SD detector is shown in the inset plot on the top right. (b) The angular resolution as a function of θ for energies exceeding 3 EeV. Image from [91].

where the shower has also been detected by the FD, the angular resolution is greatly increased to about 0.6° [91].

4.3.4 Energy estimation

After a shower core has been pinpointed and the shower axis was determined, all information to fit an LDF is present. The ShowerPlane Distance (SPD), the minimal separation between shower axis and station position, is calculated for each tank participating in the event and related to the integrated signal S (in units of Q_{VEM}) it received. From the so gathered lateral distribution of a shower the integrated signal S_{1000} of a hypothetical (labelled dense) station laying at $\text{SPD} = 1000 \text{ m}$ is obtained. This standardizes the comparison of results across many different events, even if a shower has only triggered few stations [92].

Due to attenuation effects in the atmosphere S_{1000} is a function of θ . It has been shown in [DarkoCIC] that by separating the θ dependence of a signal $S(\theta) = S \cdot A(\theta)$ and normalizing to a reference shower inclination, a reasonably unbiased estimator S_{38} can be recovered via a Constant Intensity Cut (CIC) as shown in Equation 4.5 and Equation 4.6.

$$f_{\text{CIC}} = \frac{S_{1000}(\theta)}{S_{1000}(\theta_{\text{ref}})} = \frac{A(\theta)}{A(\theta_{\text{ref}})}. \quad (4.5)$$

The reference angle is chosen as $\theta_{\text{ref}} = 38^\circ$, as this is the median inclination of detected events [93]. It follows

$$S_{38} = \frac{S_{1000}(\theta)}{f_{\text{CIC}}(\theta)}. \quad (4.6)$$

Further corrections are applied to S_{38} in order to counteract influence of the local weather or geomagnetic effects [93]. What remains is a shower parameter which has been sanitized as much as possible from any environmental factors, and which has a proportionality to the energy of the primary particle, as discussed in chapter 3.

The approximate relation of $S_{38}(E)$ can be inferred from hybrid measurements, where the calorimetric energy as measured by the FD is connected to S_{38} . From such datasets it follows the relation below, with the fit parameters for A, B as determined in [94].

$$E_{\text{SD}} = A (S_{38} / \text{VEM}_{\text{Ch.}})^B \quad (4.7)$$

$$\begin{aligned} A &= (1.86 \pm 0.03) \times 10^{17} \text{ eV} \\ B &= 1.031 \pm 0.004 \end{aligned}$$

4.3.5 Primary particle

The determination of the primary particle, also referred to as the mass composition, relies on the systematic differences in air showers discussed in section 3.3. Muons, due to their noninteracting nature at high energies are typically the first signal to arrive in a WCD from an air shower. Since high-mass primaries produce a higher fraction of muons this implies that the rise time, in which the integrated signal goes from 10% to 50% of the total received signal, is shorter in these showers. Consequent analysis over a statistically relevant dataset thus reveals the mass composition of the cosmic ray flux (compare [95], Figure 2.4)

5 Neural networks

The idea of a Neural Network (NN) is to attempt to capture the human thinking process in machine code. For this purpose, a network architecture connects some input (e.g. a picture) to an output (e.g. digits 0-9). Much like in a human brain, the architecture consists of multiple smaller chunks, neurons and layers, which connect in some way to form an emergent intelligent system.

As described, neural networks do not yet hold the abilities to achieve their designated tasks, and can hardly be called intelligent. They need to be trained. This is done by presenting an example input (called training data) to the network. The network output is compared to the desired output for the given input via some loss function. During training, the network attempts to minimize this loss function. How it is minimized is often a design choice, and in general will depend on the network architecture, which in turn is influenced by the type of data and kind of task the NN should accomplish.

In the following several network architectures which are relevant for this work are detailed. The most simple option of a Dense NN (DNN) is given in section 5.1 in order to introduce several key concepts. Convolutional NNs (CNNs) used for example in image recognition are explained in section 5.2. Lastly Recurrent NNs (RNNs) that find an application in time series analysis are shown in section 5.3

5.1 Dense neural network

Dense neural networks are subdivided into layers, which themselves consist of individual neurons. Each neuron conglomerates information from a previous layer according to some weights w_{jk} and a bias b_j and propagates it through some nonlinear activation function $\sigma^{(i)}$. That is, the propagation of an input to the output layer through intermediate, hidden layers $\mathcal{L}^{(i)}$ can be described with the below matrix form:

$$\mathcal{L}_j^{(i)} = \sum_{k=0}^{n^{(i-1)}} \sigma^{(i)} \left(w_{jk} \mathcal{L}_j^{(i-1)} + b_j \right). \quad (5.1)$$

In Equation 5.1 $\mathcal{L}_j^{(i)}$ is the value of neuron j in layer i , and $n^{(i)}$ is a reference to the number of neurons in layer i . The activation function achieves two important goals. First, it limits the numerical value neurons can have. This ensures numerical stability during training, and is typically achieved by choosing a sigmoidal activation function. Secondly, the nonlinearity of the activation function ensures that the propagation

function of the entire network cannot mathematically be reduced to a single layer, as this disallows the network to learn nonlinearly separable patterns [96].

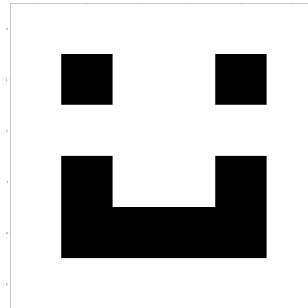
Important to note is the fact that the usage of one densely connected layer does not restrict the network architecture to consist solely of such layers. In fact, the network architectures discussed here and in the following section can all be used interchangably. This is a common practice in model building [97, 98].

5.2 Convolutional neural network

Convolutional neural networks introduce convolutional layers, which aggregate information from nearby input values. Nearby in this case referring for example to proximate pixels in a 2D image, or neighbouring voxels in a 3D scan. Even successive inputs in a 1-dimensional time series can be convoluted. In general, the working principle of a convolutional layer can be extended to an arbitrary input shape and size, but will be representatively explained here for a two-dimensional, image-like input.

The convolution in a single layer is done by one or several filters, matrices, that are scalar-multiplied to subchunks of the input data. For example a mock filter like

$$\mathcal{F} = \begin{pmatrix} -1 & -1 & -1 & -1 & -1 & -1 \\ -1 & +1 & -1 & -1 & +1 & -1 \\ -1 & -1 & -1 & -1 & -1 & -1 \\ -1 & +1 & -1 & -1 & +1 & -1 \\ -1 & +1 & +1 & +1 & +1 & -1 \\ -1 & -1 & -1 & -1 & -1 & -1 \end{pmatrix}$$

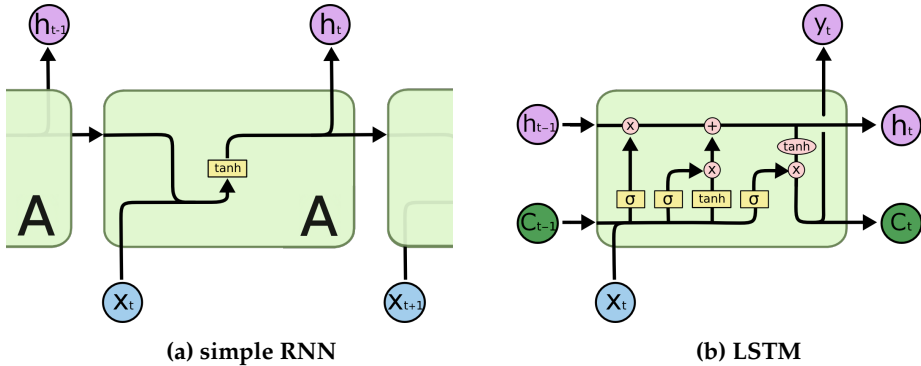


could be swept across an entire image area. During the iteration, areas of the image that resemble the filter will result in a large (relative to the input data) positive scalar value.

In this fashion, an image can be efficiently scanned for specific patterns (lines, edges, etc.) with just few parameters. Namely, these are the numerical values in the filter matrices, which can be optimized during training. The resulting output of a single layer containing different filters can interatively be propagated into subsequent convolutional layers (searching for curves, corners, etc.) until full-scale image detection of complex structures becomes possible.

5.3 Recurrent neural network

Recurrent neural networks not only propagate an input value forward through their architecture, but also introduce cyclic connections between distinct layers. For example,



a) An example RNN architecture, with one layer A, where the network output h_t at step t is used as an additional input for step $t + 1$. Image altered from [100]. **b)** The architecture of a single LSTM layer relies on multiple gates, that update the network configuration, or memory of the layer. From [100] with changes. .

in the simplest conceptional case there exists a feedback loop that connects the output of a single network layer to its' input(c.f. Figure 5.2a). Other feedback configurations are of course possible, and generally preferred, as they can address the problem of vanishing/exploding gradients [99].

Moreover, due to the cyclic connections in the network architecture, RNNs are especially qualified for time-series analysis. i.e. where temporally successive inputs are highly correlated. A popular example is the **Long Short-Term Memory (LSTM)** architecture, which is visualized in Figure 5.2b.

The output of a single LSTM layer at timestep $t \neq 0$ is calculated from two variables, the hidden state h_t , as well as the cell state C_t . The former exists in some form in every RNN, while the cell state C_t corresponds to a long-term memory that is unique to the LSTM architecture [101]. Unlike the name implies, the hidden state corresponds to the output of the network, and is thus in no way hidden. Due to vanishing/exploding gradients, the hidden state does not preserve information for more than few iterations. For this reason, it is often referred to as the short-term memory of the network. Data propagates through an LSTM layer according to the below steps (c.f. as well Figure 5.2b):

- A sigmoid layer outputs a number between 0 and 1 depending on the input x_t . The cell state from the previous iteration, C_{t-1} , is weighted by this number. In this fashion, the network can choose to discard or keep information from previous iterations. The first sigmoid layer is thus aptly named the forget gate.
 - Next, the new cell state is calculated by extracting important information from the input. This is achieved via a feature extraction layer, which is weighted by another instance of a sigmoidal layer. The thus recovered new long term memory is added to the weighted cell state C_{t-1} and represents the new cell state C_t . This is the input gate of the LSTM.
 - Lastly, the hidden state h_t is computed at the output gate of the LSTM. A feature extraction layer processes C_t and provides an output, that is weighted by one last sigmoid layer dependant on the input x_t .

5.4 Other architectures

With the current rise of deep learning applications in every facet of data processing, a plethora of other architectures have been established to achieve specific tasks. Some of these are purely generative (e.g. Generative Adversarial Networks (GANs) [102]) or not out of the box suitable for classification due to other reasons. Of particular interest, specifically for this work, are architectures that have been shown to outperform others in time-series analysis. Apart from the LSTM discussed in section 5.3 the Gated Recurrent Unit (GRU) [103] is a popular implementation of a recurrent neural network. Last but not least, transformers [104] have consistently been among the most promising architectures for time-series analysis. However, because they require a lot of computational resources they are not compatible with the use-case that this work is pertaining to.

6 Neural network training data

Over their relatively brief existance, neural networks have been shown to perform increasingly impressive tasks (e.g. [105], [106], and many more). However, they learn by example. The performance of a neural network is directly linked to the input data it receives during training. If the training data is not an accurate example of real world information a network later operates on, insight gained from it is at best an approximation, and at worst completely randomly generated data.

As such, it is not a question *if* some neural network architecture can learn to identify an extensive air shower from WCD data, but rather which implementation, fed with which information, does. For this purpose, this chapter explains the procedure with which training data is generated. As stated above, this must occur with a focus on being representative of data actually measured in the SD array. The elected approach to create time traces is modularized. The structure of this chapter reflects this. First, general comments about the characteristics of background data (i.e. the WCD detector response in the absence of an extensive air shower) are made in section 6.1. Next, the process to extract signal originating from CRs is detailed in section 6.2. Lastly, building the time trace from the aforementioned modules and drawing samples from it for a neural network to train on is done in section 6.3 and ??.

6.1 Background dataset

While a flux of particles causes elevated ADC levels in both the HG and LG channels of a WCD PMT during a shower event, the lack of such a phenomenon does not imply the readout information is uniformly flat. Instead, it hovers around the channels' baseline (c.f. section 4.2) with occasional spikes upwards due to low-energy particles impinging on the detector. Coupled with electronic noise from the many digital components in the station electronics, the **Upgraded Unified Board** (UUB), this constitutes the data that is collected inbetween air shower events.

6.1.1 Accidental muons

Most low-energy background particles present in the detector are muons. These are produced in the upper atmosphere during cascading processes analog to chapter 2. Due to the low primary energy the electromagnetic component of the shower is thermalized before it reaches surface level. The muonic component by itself does not contain enough information to enable an accurate reconstruction of primary energy and origin. This fact, coupled with the high flux of events at lower energies ($\Phi|_{E=100\text{ GeV}} \approx 1\text{ m}^{-1}\text{ s}^{-1}$

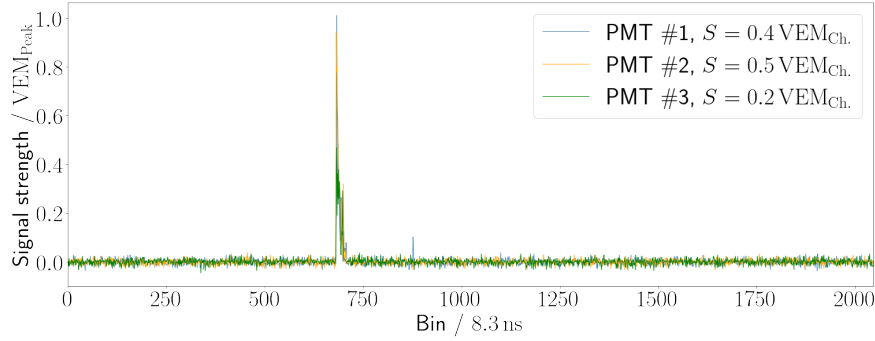


Figure 6.1: The simulated time trace from a single muon. The maximum peak of the time trace is equal to 1 VEM_{Peak}. The integral over each PMT, S , sums to ≈ 1 VEM_{Ch.}.

[107]) make these events unsuitable for analysis. Stray muons, even though they originate from extensive air showers, must consequently be considered background events.

The rate at which such particles traverse a WCD tank is $f_{\text{Acc.}} \approx 4.665 \text{ kHz}$ [108]. Their arrival time is Poisson-distributed. This implies that generally, one in 14 time traces contains signal from a low-energy background event. Coincidences of two accidental muons occur on a sub-percent level. Any higher order of coincidences is likely originating from a single air shower process. The typical signal recorded by the surface detector from a single muon is presented in Figure 6.1.

A library of background traces of this type was provided by David Schmidt [108]. However, only the largest response of the three WCD PMTs is available for this library. Due to the lack of information one is either forced to assume the response to a low-energy background particle is the same across all PMTs, or neglect the response of the two remaining PMTs altogether upon injecting a background muon into a signal trace (c.f. section 6.3). In both cases, neural networks are provided an easily detectable pattern to discern such particles from "real" shower signal. As a result, it should be refrained from training AI triggers on this dataset.

6.1.2 Electronic noise

Electronic noise is the umbrella term given to the distortions that some signal is subject to during digital readout. Such noise can have many different origins. An illustrative example is given by the **Laser Interferometer Gravitational wave Observatory**, which excludes the 60 Hz band and its' harmonics from analysis. This is owed to the fact that the DC frequency standard in the United States introduces systematic uncertainties in the detector [109]. In the electronics of Pierre Auger's SD array, electronic noise is assumed to be Gaussian. That is to say that the ADC values of a time trace that was measured while no particle produced signal in the tank are normally distributed around the baseline. The standard deviation can be estimated from monitoring data, as is shown in Figure 6.2.

6.1.3 Random traces

Both above mentioned phenomena can be simulated, and the simulation results used as background training data for the neural networks discussed in the next chapter. A more accurate method however, and the approach elected for this work is to utilize directly measured data from the field. Thanks to the work of David Nitz, there exist collections of so called random-traces¹ that were gathered by forcing DAQ readout via a manually set trigger.

In particular, two datasets of UUB random-traces have been created until now. They were taken from 13th-18th March 2022, and 14th-18th November 2022 respectively. The first set contains data a total of sixteen million time traces distributed over four different SD stations. For reasons explained in subsubsection 6.1.3, only data from the first set is used in the analysis presented in this work.

Characteristics

Contrary to the naming of the random trigger, it occurs at a deterministic time. More accurately, the process of measuring random-traces is as follows; A single time trace ($2048 \cdot 8.333 \text{ ns} = 17.07 \mu\text{s}$) is written to the local station buffer every 10 ms. Once the buffer has accumulated enough data, it is written to a USB storage device. Because of a bottleneck in the last step, the process takes about 22 h per station [110].

It is thus not the trigger that is unpredictable, but the data measured by each trigger. Due to the read/write process being independent of the measured data (as opposed to the algorithms in chapter 7) the latter must be considered to be essentially random. For the most part, random-traces are assumed to consist solely of electronic noise. However, signal of cosmic origin - be it accidental muons or extensive air showers - will appear in the data at a rate at least consistent with section 7.2.

A crude analysis of the type of noise in the random-traces can be made by examining the spectral density of the dataset, shown in Figure 6.2. Harmonic modulations visible in both spectra might originate from an offset between last and first bin of the random-traces. If this offset is nonzero, the periodic extension of $f(x)$ exerts a step-function-like behaviour. The Fourier transform consequently reflects this [111]. Still, several features of $|\hat{f}(\xi)|^2$, especially present at 10 MHz, imply the presence of systematic noise in the UUB. Nevertheless, the large scale form of the spectral density is compatible with at least two noise models, that cannot be distinguished based on the data at hand:

- $|f(\xi)|^2 \propto \exp\left(\frac{(\xi-\mu)^2}{2\sigma^2}\right)$. The spectral density is Gaussian. This implies the noise is Gaussian distributed as well, confirming the assumption in subsection 6.1.2.
- $|f(\xi)|^2 \propto \exp(-m\xi + b)$. The spectral density is proportional to ξ^{-n} for some power n . The case $n = 2$ (-6 dB/Oct attenuation) seems to describe the observations well, hinting that the generating function could be Brownian.

¹to avoid possible confusion between this dataset and a *random* trace in the statistical sense, the traces recorded by David Nitz are referred to as random-trace, with a hyphen.

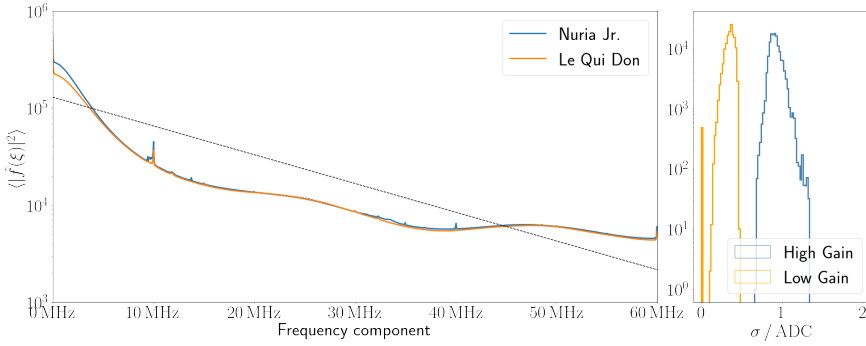


Figure 6.2: (Left) The random-trace spectral density for two stations. Plotted with a dashed black line is reference attenuation curve falling at -6 dB/Oct . The spike at 10 MHz is of unknown origin and represents systematic noise in the UUB electronics. (Right) Example variance of all UUB stations in the surface detector array. The data shown in this plot was recorded on November 15th 2022.

Calibration

The random-trace files contain raw measurement data in units of ADC for the HG and LG channel of the three WCD PMTs. In a first step to standardize this information, the baseline is subtracted from each FADC bin. This is done via the baseline finding algorithm described in subsection 4.2.2 and [86, 87]. Note that this approach differs from the baseline finding algorithm that runs on each station (c.f. subsection 4.2.3). However, the difference is negligible ($\ll 1 \text{ ADC}$) for traces that do not contain any signal, which is the case for the vast majority of the dataset.

Next, the baseline-subtracted time traces are converted from units of ADC to $I_{\text{VEM}}^{\text{Peak}}$. This conversion is not straight forward, as it requires knowledge of I_{VEM} at the time of data taking. Each station estimates this value in periodic time intervals in the context of monitoring diagnostics.

For the second dataset of random-traces (taken from 14th-18th November 2022) a UNIX timestamp packaged with each time trace may be related to monitoring data. This reveals that no information regarding I_{VEM} was forwarded to CDAS for any station while it recorded random-traces. As a result, the entire dataset is unfortunately rendered useless for this work.

For the first collection of random-traces, monitoring data is available, but there exists no timing information for the individual traces. Only the date of the measurement is known. The elected procedure to evaluate data as accurately as possible is thus to calculate the day average of I_{VEM} and Q_{VEM} and take this as the best (first) estimate for each trace. As can be seen in Figure 6.4, this eliminates half of the remaining dataset, as two of the four stations show a large variance in I_{VEM} . The day average in these particular cases is not a good estimator for calibration purposes. For this reason, only random traces from the stations Nuria and Le Qui Don, measured in the March dataset are used for analysis purposes, as their $I_{\text{VEM}, \text{Rand}}$ is stable.

Table 6.1: Calibration constant I_{VEM} for random-traces.

PMT #	Nuria	Le Qui Don
1	159.34 ADC	145.79 ADC
2	161.37 ADC	144.63 ADC
3	149.91 ADC	154.62 ADC

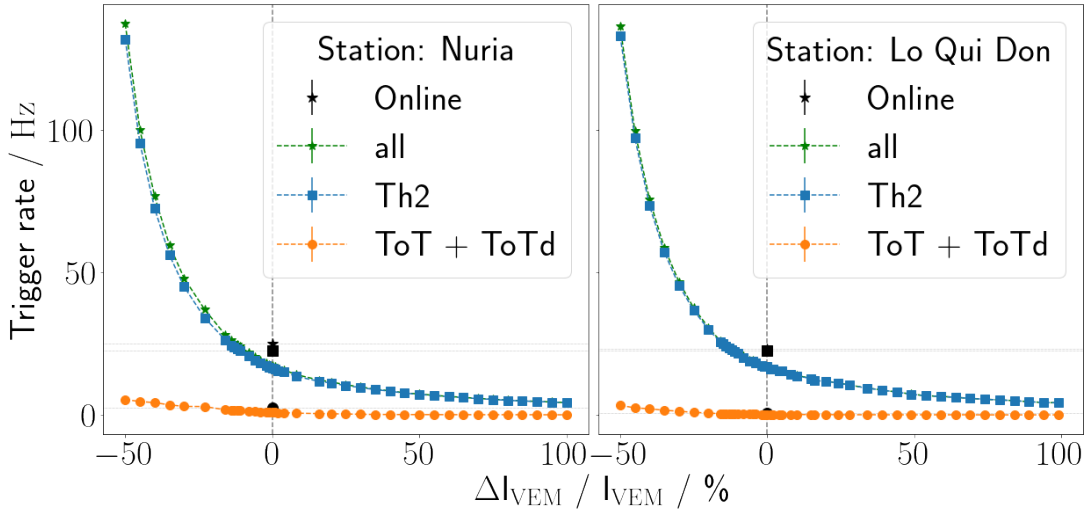


Figure 6.3: The online reported T2 trigger rate (black) does not match the calculated trigger rate. Only a decrease ΔI_{VEM} by 1/10th of the original I_{VEM} gives a close approximation of the observed rate when manually calculating trigger frequencies.

As a crosscheck to verify the goodness of the approximation, the T2 trigger rate as reported by the calibration process is related to the trigger rate obtained by direct calculation over all (calibrated) random-traces. By extension, this also serves as a unit test for the classical triggers as they will be implemented in chapter 7. The results of this analysis are shown in Figure 6.3. As is clear from the plot, the rates calculated from the two different approaches are not in accordance. This indicates systematic errors in the calibration (a wrong implementation of trigger algorithms is disfavoured from the discussion in chapter 7). The errors are consistent across both considered stations. It is found that calculated trigger frequencies are $\approx 25\%$ lower than what is taken from monitoring. It is unclear why this discrepancy occurs, as it implies that the stations do not use the same threshold values for triggering as they report.

In any case, $I_{VEM, \text{Rand.}}$ must be adjusted to reflect this. A 25% increase in trigger rate is relatable to a $\approx 10\%$ decrease in I_{VEM} . The calibration scaling factors for random-traces thus become the values listed in ??.

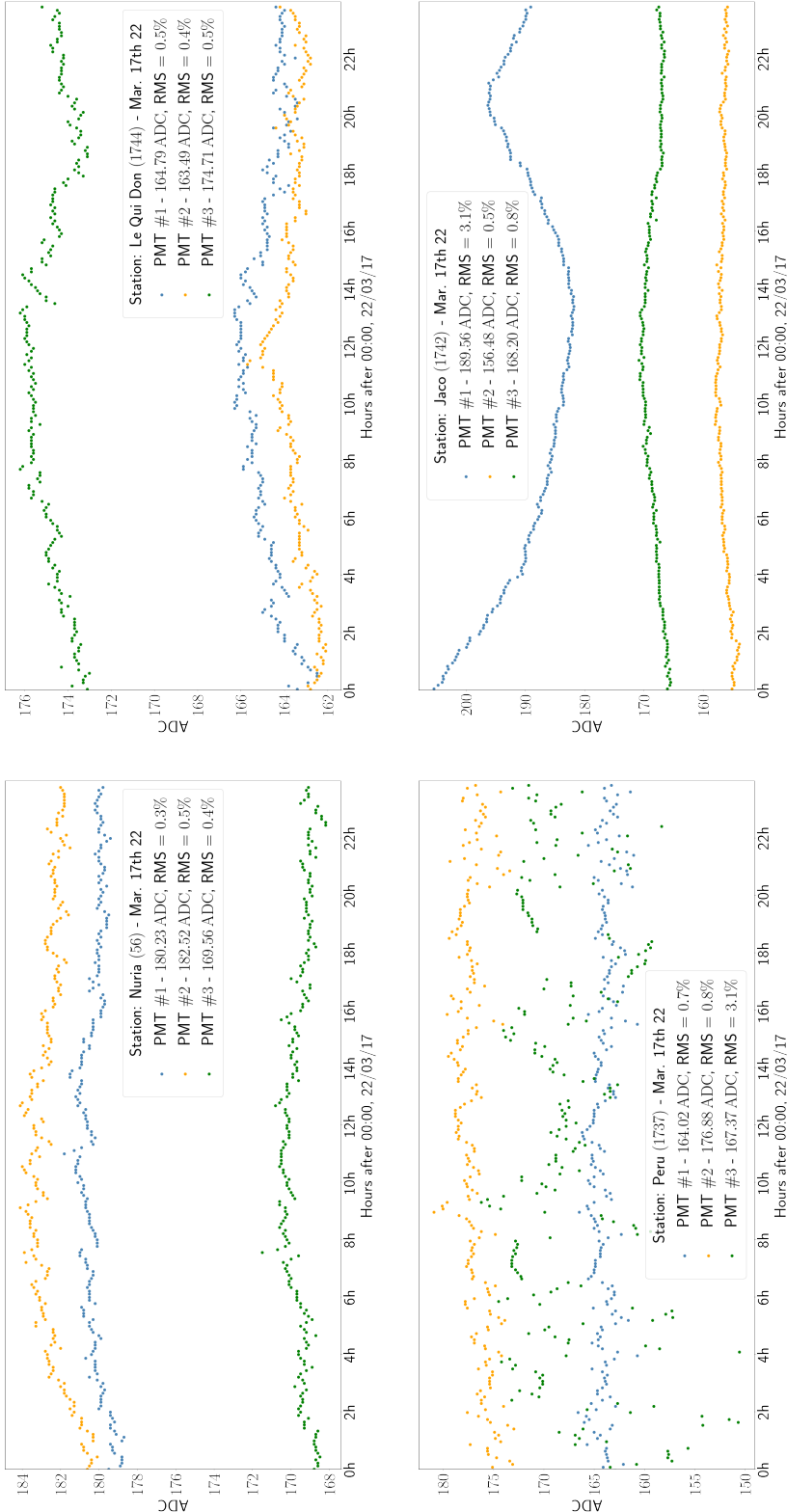


Figure 6.4: Monitoring values for the four stations available in the random-trace dataset measured in March '22. The bottom two stations show a large variance in I_{VEM} for at least one PMT. The two stations in the first row (Nuria, Le Qui Don) are more stable ($\sigma / \mu < 1\%$).

6.2 Signal dataset

In the context of this work, a "signal" (as opposed to background) is *any* detector response caused by extensive air showers. Admittedly, this choice of classification is not ideal, as the particle density far from the shower axis grows sparse. Time traces recorded at those locations look very similar to ones raised by accidental muons. In any case, ramifications and possible solutions to this problem are further discussed in the following chapters.

In order to isolate the signal stemming from shower particles only, an Offline simulation using Geant4 is executed on CORSIKA source files [56]. These are a total of 40557 simulated showers with a proton primary of energy $16 < \log(E/\text{eV}) < 19.5$. All showers are simulated using the hadronic interaction model QGSJET-II.04 [5].

In the process, the electronic feedback of the WCD PMTs is evaluated without any disturbance factor (see section 6.1). That is to say that the time trace obtained from such simulations is identically zero (in units of ADC) at any point in time where no ionizing particles are present in the WCD. An example trace that visualizes this is shown in Figure 6.5. Next, the trigger conditions both for individual stations and on the event-level are altered to trigger on everything. This step is needed in order to save all traces to the simulation output, an **Advanced Data Summary Tree** (ADST). If this was not the case, only traces that already satisfy current trigger conditions would be written to disk. A neural network training on such data could therefore at best be as efficient as the current triggers.

The choice of this approach forces some detours in the ADST readout. Instead of extracting the VEM calibrated traces directly, individual component traces, i.e. the PMT signal caused by muons, electrons and photons individually are summed to yield a total ADC trace. Signal stemming from hadrons or other components in the cascade is neglected. This does not impose any errors in the analysis, as the hadronic component especially lays close to the shower core, where the EM- and muonic component of the shower alone should already enable easy detection. Finally, the total trace as calculated above is extracted to a more easily accessible data format alongside shower metadata like primary energy, zenith, but also SPD, and particle count in the station the trace was recorded from.

6.3 Trace building

With the componentwise traces at hand, the total trace as would be recorded in the WCD PMTs for a given event, can be constructed. First, a trace container with default UUB trace length ($2048 \text{ bins} \cdot 8.3 \text{ ns / bin} = 17.07 \mu\text{s}$) and three components per bin (the three WCD PMTs) is initialized with all values equal to zero. Next, an arbitrary random-trace is selected as baseline. Since the FPGAs fundamentally count in the integer domain, the ADC data in the random-trace contains only whole numbers. As is, this wouldn't correctly model rollover when adding integer random-traces to floating point simulation information. There two ADC signals by themself

might not exceed the threshold to cross to the next higher value, but the sum would; $\lfloor 0.7 \text{ ADC} \rfloor + \lfloor 0.4 \text{ ADC} \rfloor = 0 \text{ ADC} \neq 1 \text{ ADC} = \lfloor 0.7 \text{ ADC} + 0.4 \text{ ADC} \rfloor$. To account for this, uniformly distributed random numbers from 0 (inclusive) to 1 (exclusive) are added to the random-trace.

Furthermore the $I_{\text{VEM, Rand.}}$ from random-traces (c.f. subsection 6.1.3) will in general be different from I_{VEM} simulated by $\overline{\text{Offline}}$ ($I_{\text{VEM, Off.}} = 215.781 \text{ ADC}$ compare [85]). Thus the random-trace must be scaled by a factor $\frac{I_{\text{VEM, Off.}}}{I_{\text{VEM, Rand.}}}$ before being added to the container.

If desired, accidental muons can be added to the trace container as well. This is done either by directly specifying a number of random injections, or throwing the dice according to the injection frequency specified in subsection 6.1.1. If the number of accidental muons is nonzero, a sample of random background traces from [108] is drawn and each sample added to every PMT at a random uniform position somewhere in the trace. Figure 6.5 shows an example where five muons are injected into the trace.

Last, the actual shower signal is added to the trace container. In principle, it can be added at any random position, similar to the random injections. However, for continuity reasons and ease of comparing to plots generated with other software, the latch bin for signal insertion is hardcoded to be the same as in $\overline{\text{Offline}}$, bin 660. Since otherwise the data is in the correct ADC format, no further manipulation of the data is necessary.

The trace container now holds all necessary components together, but remains in units of ADC. To convert to $V_{\text{EM, Peak}}$, each bin in each PMT trace is floored to mimic the FPGA digital counting, and divided by the appropriate scaling factor I_{VEM} . If traces need to be UB compatible the trace must be filtered and downsampled in an intermediate step. This influences the scaling factor $I_{\text{VEM, compat.}}$ in a major way (compare subsection 6.3.1). If the so-called full-bandwidth, UUB time trace is analyzed, the appropriate factor becomes $I_{\text{VEM, Off.}}$.

6.3.1 Filtering and downsampling

Although the triggers discussed in the next chapter are meant to function completely autonomously in the SD field, their implementation requires some prior knowledge of the signal one desires to detect. For their use in the Auger observatory, several hyperparameters such as the thresholds of the Th-Trigger, or the window size of the ToT-trigger have been determined in studies ([112], [113], [114]).

These studies were conducted using the predecessor, the Unified Board (UB), of the hardware that is being installed during the AugerPrime upgrade of the observatory. Most importantly, the UUB has a sampling rate that is three times larger (120 MHz) than that of UB electronics (40 MHz). Not only does this raise the number of bins in a standard time trace from 682 to $2^{11} = 2048$, but also drastically reduces the efficiency (in particular for ToT-like triggers) of the above discussed algorithms. Whereas a new

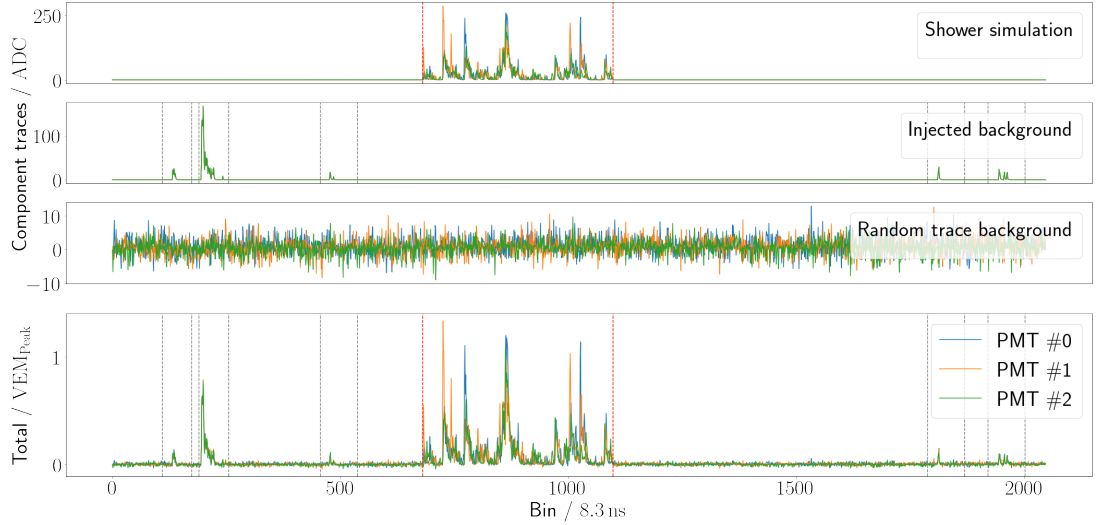


Figure 6.5: The individual component traces (in units of ADC, top three plots) make up the eventual VEM trace (in VEM_{Peak} , bottom plot). The dashed red (gray) lines signify where in the time trace the shower signal (injected muon signal) is located.

bin is measured every 25 ns in a UB station, the triggers would receive a new input every ≈ 8.3 ns in a UUB setting.

The modus operandi elected by the Pierre Auger collaboration to circumvent this problem is to emulate UB electronics using the UUB electronics. This means that measured FADC bins are to be filtered and downsampled before any trigger runs over them. Software implementations by which this is achieved are listed in ?? . The effect the filtering and downsampling has on measured data is visualized in Figure 6.6.

While the features of the time trace largely remain intact, the absolute signal strength decreases due to a smearing effect imposed by the filtering. Overall, this amounts to a 30% difference in amplitude between UUB full-bandwidth traces and their filtered and downsampled counterpart. Since both measurements are derived from the same signal in the WCD though, this implies that I_{VEM} must be adjusted by 30% as well, if traces are to be downsampled. This results in a compatibility scaling factor $I_{VEM, \text{compat.}} = 163.235 \text{ ADC}$ [OfflineSource].

Recent contributions within the Auger collaboration ([115, 116]), and to some extent also this work have shown that issues arise in the comparison of Lateral Trigger Probabilities (LTPs) that are run in this compatibility mode. Namely, the UUB trigger efficiency (where full-bandwidth traces are filtered and downsampled) is lower than that of UB stations. This implies that the filtering and downsampling algorithms in ?? either make imprecise assumptions about the station electronics, or $I_{VEM, \text{compat.}}$ or the trigger thresholds themselves need to be adjusted further. This fact has to be kept in mind when discussing results and comparing lateral trigger probabilities from classical triggers and neural networks.

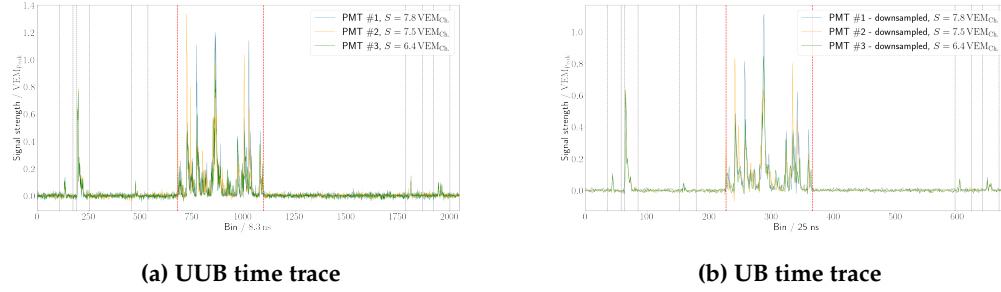


Figure 6.6: (a) A simulated signal as it would appear to UUB electronics. The ionizing particles originating in the extensive air shower hit the tank around bin 660 ($\approx 5.5 \mu\text{s}$). (b) The same signal but filtered and downsampled to emulate UB electronics.

6.3.2 Sliding window analysis & Labelling

As will become apparent in chapter 7, three of the four trigger algorithms operate by examining only a window of measurement info, rather than evaluate the whole time trace as it is constructed in section 6.3. In a similar fashion, it is reasonable to assume neural networks do not need to receive the $3(\text{PMT}) \cdot 2048(\text{UUB bins}) = 6144$ input values from the entire trace to make an informed choice of whether or not a given signal stems from an extensive air shower.

For this reason, samples from the time trace are drawn via a sliding window analysis. A number of n_{bins} are extracted from the trace, to be analyzed by some classification algorithm. In order to not select the same information repeatedly, the window is moved by n_{skip} bins forward and the process can begin anew. Unless explicitly specified otherwise, the hyperparameters in this sliding window analysis are set as

$$n_{\text{bins}} = 120, \quad n_{\text{skip}} = 10. \quad (6.1)$$

Whether or not a specific window contains signal from an extensive air shower - which is important for labelling data in the context of neural network training - is a simple exercise. The modular approach in section 6.3 allows to simply check for nonzero bins in the shower signal component of the trace. In practice, upon creating a new combined trace, the first and last positive bin in the shower component are identified. This is e.g. visualized with dashed red lines in Figure 6.5. If any overlap - even just a single bin - exists between the sliding window and this signal region, the extracted window is consequently labelled as signal. If this is not the case, the window is labelled as background.

Of course, quality cuts can be applied, and a decision to count a given trace window can be made individually. This is further discussed in ??.

7 Classical station triggers

As mentioned in chapter 4, continuously analyzing data sent to CDAS from each of the 1600 SD water tanks would quickly exceed the computational capabilities of Auger's main servers. For this purpose, trace information is only collected from a station, once a nearby T3 event (c.f. subsubsection 4.3.1) has been detected. The formation of a T3 trigger is dependant on several T2, or station-level, triggers, which will be discussed in detail in this chapter. First, the implementation of different trigger algorithms is discussed in section 7.1. Their performance is evaluated in section 7.2.

7.1 Implementation

7.1.1 Threshold trigger (Th)

The Threshold trigger (Th) is the simplest, as well as longest operating trigger algorithm [117] in the field. It scans incoming ADC bins as measured by the three different WCD PMTs for values that exceed some threshold. If a coincident exceedance of this threshold is observed in all three WCD PMTs simultaneously, a Th-T1/2 trigger is issued. A pseudocode implementation of this algorithm is hence given by the below code block.

```
1 th1 = 1.75 // Th1 level threshold above baseline, in VEM
2 th2 = 3.20 // Th2 level threshold above baseline, in VEM
3
4 while True:
5
6     pmt1, pmt2, pmt3 = get_next_output_from_WCD()
7
8     if pmt1 <= th2 and pmt2 <= th2 and pmt3 <= th2:
9         raise ThT1_trigger
10    if pmt1 <= th1 and pmt2 <= th1 and pmt3 <= th1:
11        raise ThT2_trigger
12    else:
13        continue
```

Logically, with increasing signal strength S in the PMTs, the likelihood of having observed an extensive air shower raises. This is reflected in the trigger level logic, where a coincident signal of $S \leq 3.20 \text{ VEM}_{\text{Peak}}$ is immediately forwarded to CDAS, whereas a signal $1.75 \text{ VEM}_{\text{Peak}} \geq S < 3.20 \text{ VEM}_{\text{Peak}}$ only raises a Th-T1 trigger. The algorithm is insensitive to signals that do not exceed at least 1.75 VEM_{Peak} in all three PMTs.

In the case of faulty electronics, where only a subset of the WCD PMTs are available, the trigger thresholds (in units of VEM_{Peak}) are updated according to Table 7.1.

Table 7.1: Numerical values from [113]

nPMT	Th-T2	Th-T1
1	5.00	2.85
2	3.60	2.00
3	3.20	1.75

7.1.2 Time over Threshold trigger (ToT)

The Time over Threshold trigger (ToT) is sensitive to much smaller signals than the Threshold trigger discussed in subsection 7.1.1. For each PMT in the water tank, the past 120 bins are examined for values that exceed 0.2 VEM_{Peak}. If 13 or more bins above the threshold are found in the window - ordering or succession do not matter - the PMT is considered to have an elevated pedestal. The ToT trigger requires at least two PMTs with an elevated pedestal in order to activate. As such, the algorithm is theoretically sensitive to events that deposit just 0.5 VEM_{Ch}. A pseudocode example is given below.

```

1  threshold    = 0.2 // pedestal threshold, in VEM
2  n_bins       = 12  // number of bins above pedestal
3  window_size  = 120 // considered window length
4
5  buffers = [[False for i in 1..window_size] for j in 1..3]
6  step_count = 0
7
8  while True:
9
10     pmts = get_next_output_from_WCD()
11     buffer_index = step_count % window_size
12     count_active_PMTs = 0
13
14     for pmt, buffer in pmts, buffers:
15         if pmt <= threshold: buffer[buffer_index] = True
16
17         if count_values(buffer, value = True) > n_bins:
18             count_active_PMTs += 1
19
20     if count_active_PMTs >= 2:
21         raise ToTT2_trigger
22     else:
23         step_count = buffer_index + 1
24         continue

```

7.1.3 Time over Threshold deconvoluted trigger (ToTd)

An extension to even lower signal strengths is given by the **ToT-deconvoluted trigger** (ToTd). As the name implies, the implementation of the algorithm is completely analog to the ToT trigger in subsection 7.1.2. Only the FADC input stream from the three PMTs is altered according to Equation 7.1.

$$d_i = (a_i - a_{i-1} \cdot e^{-\Delta t/\tau}) / (1 - e^{\Delta t/\tau}) \quad (7.1)$$

In Equation 7.1, the deconvoluted bin d_i is calculated from the measured FADC values a_i and a_{i-1} , where a_{i-1} is scaled according to an exponential decay with mean lifetime $\tau = 67$ ns. This reduces the exponential tail of an electromagnetic signal to a series of pulses which in the case of $a_{i-1} < a_i$ exceed the original signal strength. As such, the deconvoluted trace can satisfy the ToT trigger requirements, whereas the original raw FADC values might not have, extending the sensitivity of the ToT trigger to lower signal strengths. The scaling constant $\Delta t = 25$ ns is tied to the sampling rate of UB electronics (c.f. subsection 4.2.1). The choice of the numerical constants τ and Δt is explained in more detail in [118].

7.1.4 Multiplicity of Positive Steps (MoPS)

The **Multiplicity of Positive Steps** (MoPS) algorithm triggers on positive flanks of an FADC trace, which can be related to the arrival of new particles in the water tank.

A positive flank in the FADC trace of a single PMT is any combination of at least two bins that are monotonically increasing in value, in a window of 120 bins. Once such a positive step has been identified, a (MoPS) trigger veto is applied to the next

$$n_{\text{skip}} = \lfloor (\log_2(\Delta y) + 1) - 3 \rfloor \quad (7.2)$$

bins, where Δy refers to the total vertical increase in the step from first to last bin. Note that in Equation 7.2 the notation $\lfloor x \rfloor$ is used as shorthand notation to round x to the nearest integer. If Δy is bigger than $y_{\min} = 3$ ADC (to filter random fluctuations), but does not exceed $y_{\max} = 31$ ADC (to prevent triggering on muonic coincidences), it is added to a ledger. If the number of rising flanks in the ledger is bigger than $m > 4$ for at least two PMTs, a final check regarding the integral of the FADC trace is performed. If this check passes, a MoPS-T2 trigger is issued to CDAS. An in-depth discussion of the different hyperparameters for this trigger is offered e.g. in [119].

It is impossible to accurately recreate the MoPS trigger in simulations. The integral test above compares the sum of the last 250 bins against a threshold ($\sum a_i > 75$). Since not all 250 bin values are available to CDAS, differing results are to be expected when comparing the implementation of the algorithm in the SD field versus its' counterpart in analysis software.

For this purpose, the MoPs trigger is not considered in the analysis presented in ??.
The implications of this choice are layed out in section 7.2.

7.2 Performance

The performance of a trigger can be evaluated in many different ways. In the most general consideration, a confusion matrix holds information about the ability of a classifier to discern between different types, or classes, C . With the example at hand there exist two types of events one wishes to distinguish, a signal event C_1 in the form of an extensive air shower, versus background C_0 . The confusion matrix thus becomes:

		Predicted C	
		C_1	C_0
True C	C_1	True positive (TP)	False negative (FN)
	C_0	False positive (FP)	True negative (TN)

From this, other potentially interesting variables can be derived. Of particular interest for the Auger observatory are the sensitivity and **False Discovery Rate** (FDR). The former is the probability that a signal event will be classified correctly, i.e. an extensive air shower hits a water tank and raises a T2 trigger. The sensitivity - in the following also called the trigger efficiency ϵ - is defined as

$$\epsilon = \frac{\text{TP}}{\text{TP} + \text{FN}}. \quad (7.3)$$

The latter is a measure of how readily the triggers (wrongly) identify background events like stray cosmic muons as extensive air showers. It is imperative for any trigger algorithm operating in the SD to minimize this probability. Simply due to the number of operating stations in the field, a small increase in FDR drastically raise the amount of potential events and hence load on the central analysis server of the observatory.

$$\text{FDR} = \frac{\text{FP}}{\text{TP} + \text{FP}}. \quad (7.4)$$

7.2.1 Lateral Trigger Probability function

Ultimately, all test statistics constructed by classical station triggers (ignoring MoPS) are aliases for the deposited charge S in the WCD. Because S is heavily influenced by the primary particle energy, zenith and distance to the shower core, as well as to a lesser extent by shower age and statistical fluctuations, it makes sense to parametrize the trigger efficiency $\epsilon(E, \theta, \text{SPD})$ in terms of these observables.

From a heuristic consideration, it can immediately be concluded that large separations between station and shower axis affect efficiencies negatively, because the particle distribution function monotonically decreases with increasing r (compare Figure 3.3). Similarly, inclined showers with a large θ are more attenuated compared to vertical showers, as they have to traverse a larger atmospheric depth ($\propto \sec(\theta)$) before reaching the detector. Lastly, primaries with large E on average deposit higher S in the WCD due to unleashing bigger particle cascades. Consequently ϵ is positively correlated to E .

The functional form that can be obtained by evaluating trigger efficiencies for a given (slice of) E and θ is labelled the **Lateral Trigger Probability** (LTP). It will be the main comparison metric, by which different trigger algorithms are compared in this work. For classical triggers, two methods to extract LTPs are presented here.

Bibliography

- [1] Robert A Millikan and G Harvey Cameron. "The origin of the cosmic rays". In: *Physical review* 32.4 (1928), p. 533.
- [2] Thomas H Johnson. "A note on the nature of the primary cosmic radiation". In: *Physical Review* 54.5 (1938), p. 385.
- [3] Nobel Media AB. *Press release*. <https://www.nobelprize.org/prizes/physics/1936/summary/>. Accessed: 18th Jul. 2022. 1936.
- [4] Pierre Auger et al. "Extensive cosmic-ray showers". In: *Reviews of modern physics* 11.3-4 (1939), p. 288.
- [5] Sergey Ostapchenko. "Status of QGSJET". In: *AIP Conference Proceedings*. Vol. 928. 1. American Institute of Physics. 2007, pp. 118–125.
- [6] I Goldman et al. "Implications of the supernova SN1987A neutrino signals". In: *Physical review letters* 60.18 (1988), p. 1789.
- [7] J Abraham et al. "Measurement of the energy spectrum of cosmic rays above 10¹⁸ eV using the Pierre Auger Observatory". In: *Physics Letters B* 685.4-5 (2010), pp. 239–246.
- [8] Alexander Aab et al. "Searches for anisotropies in the arrival directions of the highest energy cosmic rays detected by the Pierre Auger Observatory". In: *The Astrophysical Journal* 804.1 (2015), p. 15.
- [9] Hannes Alfvén. "Existence of electromagnetic-hydrodynamic waves". In: *Nature* 150.3805 (1942), pp. 405–406.
- [10] Enrico Fermi. "On the origin of the cosmic radiation". In: *Physical review* 75.8 (1949), p. 1169.
- [11] AM Hillas. "Can diffusive shock acceleration in supernova remnants account for high-energy galactic cosmic rays?" In: *Journal of Physics G: Nuclear and Particle Physics* 31.5 (2005), R95.
- [12] Pasquale Blasi. "The origin of galactic cosmic rays". In: *The Astronomy and Astrophysics Review* 21.1 (2013), pp. 1–73.
- [13] Katsuaki Asano and Masaaki Hayashida. "The most intensive gamma-ray flare of quasar 3C 279 with the second-order Fermi acceleration". In: *The Astrophysical Journal Letters* 808.1 (2015), p. L18.
- [14] Ruth A Daly. "Black hole spin and accretion disk magnetic field strength estimates for more than 750 active galactic nuclei and multiple galactic black holes". In: *The Astrophysical Journal* 886.1 (2019), p. 37.

- [15] Elliott Flowers and Malvin A Ruderman. "Evolution of pulsar magnetic fields". In: *The Astrophysical Journal* 215 (1977), pp. 302–310.
- [16] FM Rieger and K Mannheim. "Particle acceleration by rotating magnetospheres in active galactic nuclei". In: *arXiv preprint astro-ph/9911082* (1999).
- [17] Zaza Osmanov, Andria Rogava, and Gianluigi Bodo. "On the efficiency of particle acceleration by rotating magnetospheres in AGN". In: *Astronomy & Astrophysics* 470.2 (2007), pp. 395–400.
- [18] Frank M Rieger. "Cosmic ray acceleration in active galactic nuclei-on centaurus a as a possible uhecr source". In: *arXiv preprint arXiv:0911.4004* (2009).
- [19] Anthony M Hillas. "The origin of ultra-high-energy cosmic rays". In: *Annual review of astronomy and astrophysics* 22 (1984), pp. 425–444.
- [20] AU Abeysekara et al. "Very-high-energy particle acceleration powered by the jets of the microquasar SS 433". In: *Nature* 562.7725 (2018), pp. 82–85.
- [21] Aya Ishihara, IceCube Collaboration, et al. "Extremely high energy neutrinos in six years of IceCube data". In: *Journal of Physics: Conference Series*. Vol. 718. 6. IOP Publishing. 2016, p. 062027.
- [22] Frank C Jones. "Inverse Compton scattering of cosmic-ray electrons". In: *Physical Review* 137.5B (1965), B1306.
- [23] Enrico Fermi. "98. Galactic Magnetic Fields and the Origin of Cosmic Radiation". In: *A Source Book in Astronomy and Astrophysics, 1900–1975*. Harvard University Press, 2013, pp. 671–676.
- [24] Matthias Bartelmann. "Gravitational lensing". In: *Classical and Quantum Gravity* 27.23 (2010), p. 233001.
- [25] Matthias Bartelmann and Peter Schneider. "Weak gravitational lensing". In: *Physics Reports* 340.4-5 (2001), pp. 291–472.
- [26] Marijke Haverkorn. "Magnetic fields in the Milky Way". In: *Magnetic fields in diffuse media*. Springer, 2015, pp. 483–506.
- [27] Pierre Auger Collaboration et al. "Observation of a large-scale anisotropy in the arrival directions of cosmic rays above 8×10^{18} eV". In: *Science* 357.6357 (2017), pp. 1266–1270.
- [28] J Skilling. "The diffusion of cosmic rays". In: *Monthly Notices of the Royal Astronomical Society* 147.1 (1970), pp. 1–12.
- [29] Leonard Searle and Robert Zinn. "Compositions of halo clusters and the formation of the galactic halo". In: *The Astrophysical Journal* 225 (1978), pp. 357–379.
- [30] Particle Data Group et al. "Review of Particle Physics". In: *Progress of Theoretical and Experimental Physics* 2020.8 (Aug. 2020). 083C01. issn: 2050-3911. doi: [10.1093/ptep/ptaa104](https://doi.org/10.1093/ptep/ptaa104). eprint: <https://academic.oup.com/ptep/article-pdf/2020/8/083C01/34673722/ptaa104.pdf>. url: <https://doi.org/10.1093/ptep/ptaa104>.
- [31] Kenneth Greisen. "End to the cosmic-ray spectrum?" In: *Physical Review Letters* 16.17 (1966), p. 748.

- [32] GT Zatsepin and VA Kuz'min. "J. of Exp. and Theor". In: *Phys. Lett* 4 (1966), p. 78.
- [33] Vadim N Gamezo, Alexei M Khokhlov, and Elaine S Oran. "Three-dimensional delayed-detonation model of type Ia supernovae". In: *The Astrophysical Journal* 623.1 (2005), p. 337.
- [34] John J Cowan and Friedrich-Karl Thielemann. "R-process nucleosynthesis in supernovae". In: *Physics Today* 57.10 (2004), pp. 47–54.
- [35] M Garcia-Munoz, GM Mason, and JA Simpson. "The age of the galactic cosmic rays derived from the abundance of Be-10". In: *The Astrophysical Journal* 217 (1977), pp. 859–877.
- [36] JZ Wang et al. "Measurement of cosmic-ray hydrogen and helium and their isotopic composition with the BESS experiment". In: *The Astrophysical Journal* 564.1 (2002), p. 244.
- [37] Michael W Kirson. "Mutual influence of terms in a semi-empirical mass formula". In: *Nuclear Physics A* 798.1-2 (2008), pp. 29–60.
- [38] Thomas K Gaisser, Ralph Engel, and Elisa Resconi. *Cosmic rays and particle physics*. Cambridge University Press, 2016.
- [39] Hans Dembinski et al. "Data-driven model of the cosmic-ray flux and mass composition from 10 GeV to 10^{11} GeV". In: *arXiv preprint arXiv:1711.11432* (2017).
- [40] Anatoly Klypin et al. "Structure formation with cold+ hot dark matter". In: *arXiv preprint astro-ph/9305011* (1993).
- [41] Fiorenza Donato et al. "Constraints on WIMP Dark Matter from the High Energy PAMELA p/p data". In: *Physical review letters* 102.7 (2009), p. 071301.
- [42] Antonella Castellina. "AugerPrime: the Pierre Auger observatory upgrade". In: *EPJ Web of Conferences*. Vol. 210. EDP Sciences. 2019, p. 06002.
- [43] Roberto Aloisio et al. "A dip in the UHECR spectrum and the transition from galactic to extragalactic cosmic rays". In: *Astroparticle Physics* 27.1 (2007), pp. 76–91.
- [44] Denis Allard. "Extragalactic propagation of ultrahigh energy cosmic-rays". In: *Astroparticle Physics* 39 (2012), pp. 33–43.
- [45] Sow-Hsin Chen and Michael Kotlarchyk. *Interactions of photons and neutrons with matter*. World Scientific, 2007.
- [46] Stefano Meroli. "The Straggling function. Energy Loss Distribution of charged particles in silicon layers". In: *Home Cern*, <https://meroli.web.cern.ch/lecture-StragglingFunction.html> (2017).
- [47] Walter Heitler. *The quantum theory of radiation*. Courier Corporation, 1984.
- [48] Koichi Kamata and Jun Nishimura. "The lateral and the angular structure functions of electron showers". In: *Progress of Theoretical Physics Supplement* 6 (1958), pp. 93–155.

- [49] Kenneth Greisen. "Cosmic ray showers". In: *Annual review of nuclear science* 10.1 (1960), pp. 63–108.
- [50] Gert Moliere. "Theorie der streuung schneller geladener teilchen i. einzelstreuung am abgeschirmten coulomb-feld". In: *Zeitschrift für Naturforschung A* 2.3 (1947), pp. 133–145.
- [51] James Matthews. "A Heitler model of extensive air showers". In: *Astroparticle Physics* 22.5-6 (2005), pp. 387–397.
- [52] Tomás Capistrán, I Torres, and L Altamirano. "New method for Gamma/Hadron separation in HAWC using neural networks". In: *arXiv preprint arXiv:1508.04370* (2015).
- [53] Fabian Schmidt. *Sample Corsika showers*. <https://www.zeuthen.desy.de/~jknapp/fs/proton-showers.html>. Accessed: 08th Dec. 2022.
- [54] Martin Pittermann and Paul Filip. *Simple hadronic shower simulation in C++*. <https://github.com/martin2250/showersim>. Accessed: 13th Dec. 2022.
- [55] Sea Agostinelli et al. "GEANT4—a simulation toolkit". In: *Nuclear instruments and methods in physics research section A: Accelerators, Spectrometers, Detectors and Associated Equipment* 506.3 (2003), pp. 250–303.
- [56] Dieter Heck et al. "CORSIKA: A Monte Carlo code to simulate extensive air showers". In: *Report fzka* 6019.11 (1998).
- [57] S Ostapchenko. "QGSJET-II: towards reliable description of very high energy hadronic interactions". In: *Nuclear Physics B-Proceedings Supplements* 151.1 (2006), pp. 143–146.
- [58] DJ Fox et al. "Early tests of scale invariance in high-energy muon scattering". In: *Physical Review Letters* 33.25 (1974), p. 1504.
- [59] Larry C Andrews. "An analytical model for the refractive index power spectrum and its application to optical scintillations in the atmosphere". In: *Journal of Modern Optics* 39.9 (1992), pp. 1849–1853.
- [60] The VERITAS Collaboration. *VERITAS Telescope Homepage*. <https://veritas.sao.arizona.edu/>. Accessed: 26th Dec. 2022.
- [61] The H.E.S.S. Collaboration. *H.E.S.S. Telescope Homepage*. <https://www.mpi-hd.mpg.de/hfm/HESS/>. Accessed: 26th Dec. 2022.
- [62] The Pierre Auger Collaboration. *Pierre Auger Observatory Homepage*. <https://www.auger.org/>. Accessed: 26th Dec. 2022.
- [63] The HAWC Collaboration. *HAWC Observatory Homepage*. <https://www.hawc-observatory.org/>. Accessed: 26th Dec. 2022.
- [64] The Kamiokande Collaboration. *Super-Kamiokande Homepage*. <https://www-sk.icrr.u-tokyo.ac.jp/en/sk/>. Accessed: 26th Dec. 2022.
- [65] Jorge Abraham et al. "The fluorescence detector of the Pierre Auger Observatory". In: *Nuclear Instruments and Methods in Physics Research Section A: Accelerators, Spectrometers, Detectors and Associated Equipment* 620.2-3 (2010), pp. 227–251.

- [66] Louis Elterman. *UV, visible, and IR attenuation for altitudes to 50 km, 1968*. Tech. rep. AIR FORCE CAMBRIDGE RESEARCH LABS HANSCOM AFB MA, 1968.
- [67] Ghouti Abdellaoui et al. "EUSO-TA—First results from a ground-based EUSO telescope". In: *Astroparticle Physics* 102 (2018), pp. 98–111.
- [68] M Nagano et al. "New measurement on photon yields from air and the application to the energy estimation of primary cosmic rays". In: *Astroparticle Physics* 22.3-4 (2004), pp. 235–248.
- [69] Ina Holl, Eckart Lorenz, and Gikas Mageras. "A measurement of the light yield of common inorganic scintillators". In: *IEEE Transactions on Nuclear Science* 35.1 (1988), pp. 105–109.
- [70] The KASCADE Collaboration. *KASCADE Homepage*. <https://www.iap.kit.edu/kascade/index.php>. Accessed: 26th Dec. 2022.
- [71] Alexander Aab et al. "Observation of inclined EeV air showers with the radio detector of the Pierre Auger Observatory". In: *Journal of Cosmology and Astroparticle Physics* 2018.10 (2018), p. 026.
- [72] The Pierre Auger Collaboration. *AERA - Auger Engineering Radio Array*. <https://auger.org/observatory/aera>. Accessed: 18th Jan. 2023.
- [73] Jaime Álvarez-Muñiz et al. "The giant radio array for neutrino detection (GRAND): science and design". In: *Science China Physics, Mechanics & Astronomy* 63.1 (2020), pp. 1–43.
- [74] Alexander Aab et al. "The pierre auger observatory upgrade-preliminary design report". In: *arXiv preprint arXiv:1604.03637* (2016).
- [75] The Pierre Auger Collaboration. *Timeline of the Pierre Auger Observatory*. <https://auger.org/observatory/timeline-observatory>. Accessed: 04th Oct. 2022. 2022.
- [76] Carola Dobrigkeit et al. "PC Status Report". Auger internal document, 13th November 2022.
- [77] Alexander Aab et al. "Reconstruction of events recorded with the surface detector of the Pierre Auger Observatory". In: *Journal of Instrumentation* 15.10 (2020), P10021.
- [78] Darko Veberič. *Auger array*. https://web.ikp.kit.edu/darko/auger/auger-array/auger_array-pdf/auger_array-ad.pdf. Accessed: 19th Jul. 2022. 2021.
- [79] The Pierre Auger Collaboration. *AugerPrime*. <https://auger.org/observatory/augerprime>. Accessed: 06th Nov. 2022.
- [80] João de Mello Neto, ed. *Physics and astrophysics of ultra-high energy cosmic rays: recent results from the Pierre Auger Observatory*. NUCLEUS - 2020.
- [81] Antonella Castellina. "AugerPrime: the Pierre Auger observatory upgrade". In: *EPJ Web of Conferences*. Vol. 210. EDP Sciences. 2019, p. 06002.
- [82] Jörg R Hörandel. "Precision measurements of cosmic rays up to the highest energies with a large radio array at the Pierre Auger Observatory". In: *EPJ Web of Conferences*. Vol. 210. EDP Sciences. 2019, p. 06005.

- [83] Valerio Verzi et al. "The energy scale of the Pierre Auger Observatory". In: *Proceedings of the 33rd ICRC, Rio de Janeiro, Brasil* (2013).
- [84] Xavier Bertou et al. "Local-Station Calibration". GAP 2022-0??
- [85] The Pierre Auger Collaboration. *Official Auger Reconstruction and Simulation Framework*. <https://gitlab.iap.kit.edu/auger-observatory/offline>. HEAD = 5f8b537e (Tue Dec 13 09:58:43).
- [86] Tobias Schulz et al. "New Baseline Algorithm for UB Traces". GAP 2022-045.
- [87] Tobias Schulz et al. "New Baseline Algorithm for UUB Traces". GAP 2023-007.
- [88] Alexander Streich et al. "Performance of the upgraded surface detector stations of the Pierre Auger Observatory". In: *Verhandlungen der Deutschen Physikalischen Gesellschaft* (2018).
- [89] P.S. Allison et al. "Surface Detector calibration in the Engineering Array". GAP 2002-028. July 2002.
- [90] J Abraham et al. "Trigger and aperture of the surface detector array of the Pierre Auger Observatory". In: *Nuclear Instruments and Methods in Physics Research Section A: Accelerators, Spectrometers, Detectors and Associated Equipment* 613.1 (2010), pp. 29–39.
- [91] C Bonifazi. "Angular resolution of the pierre auger observatory". In: *29th International Cosmic Ray Conference (ICRC29), Volume 7*. Vol. 7. 2005, p. 17.
- [92] Thomas K Gaisser and A Michael Hillas. "Reliability of the method of constant intensity cuts for reconstructing the average development of vertical showers". In: *International Cosmic Ray Conference*. Vol. 8. 1977, pp. 353–357.
- [93] Alexander Aab et al. "Measurement of the cosmic-ray energy spectrum above 2.5×10^{18} eV using the Pierre Auger Observatory". In: *Physical Review D* 102.6 (2020), p. 062005.
- [94] A. Aab et al. "Measurement of the cosmic-ray energy spectrum above 2.5×10^{18} eV using the Pierre Auger Observatory". In: *Phys. Rev. D* 102 (6 Sept. 2020), p. 062005. doi: [10.1103/PhysRevD.102.062005](https://doi.org/10.1103/PhysRevD.102.062005). url: <https://link.aps.org/doi/10.1103/PhysRevD.102.062005>.
- [95] Antoine Letessier-Selvon. "Highlights from the Pierre Auger Observatory". In: *Brazilian Journal of Physics* 44.5 (2014), pp. 560–570.
- [96] Stuart J Russell. *Artificial intelligence a modern approach*. Pearson Education, Inc., 2010.
- [97] Christian Szegedy et al. "Going deeper with convolutions". In: *Proceedings of the IEEE conference on computer vision and pattern recognition*. 2015, pp. 1–9.
- [98] Alex Krizhevsky, Ilya Sutskever, and Geoffrey E Hinton. "Imagenet classification with deep convolutional neural networks". In: *Communications of the ACM* 60.6 (2017), pp. 84–90.
- [99] Sepp Hochreiter. "Untersuchungen zu dynamischen neuronalen Netzen". In: *Diploma, Technische Universität München* 91.1 (1991).

- [100] Christopher Olah. *Understanding LSTM Networks*. <https://colah.github.io/posts/2015-08-Understanding-LSTMs/>. Accessed: 11th Mar. 2023. Aug. 2015.
- [101] Felix A Gers, Jürgen Schmidhuber, and Fred Cummins. “Learning to forget: Continual prediction with LSTM”. In: *Neural computation* 12.10 (2000), pp. 2451–2471.
- [102] Antonia Creswell et al. “Generative adversarial networks: An overview”. In: *IEEE signal processing magazine* 35.1 (2018), pp. 53–65.
- [103] Rahul Dey and Fathi M Salem. “Gate-variants of gated recurrent unit (GRU) neural networks”. In: *2017 IEEE 60th international midwest symposium on circuits and systems (MWSCAS)*. IEEE. 2017, pp. 1597–1600.
- [104] Ashish Vaswani et al. “Attention is all you need”. In: *Advances in neural information processing systems* 30 (2017).
- [105] OpenAI et al. *Dota 2 with Large Scale Deep Reinforcement Learning*. 2019. arXiv: 1912.06680 [cs.LG].
- [106] OpenAI. *GPT-4 Technical Report*. 2023. arXiv: 2303.08774 [cs.CL].
- [107] M Boezio et al. “Measurement of the flux of atmospheric muons with the CAPRICE94 apparatus”. In: *Physical Review D* 62.3 (2000), p. 032007.
- [108] David Schmidt. *Background Simulation library*. personal communication. June 2022.
- [109] Denis V Martynov et al. “Sensitivity of the Advanced LIGO detectors at the beginning of gravitational wave astronomy”. In: *Physical Review D* 93.11 (2016), p. 112004.
- [110] David Nitz. *Random trace characteristics*. personal communication. Sept. 2022.
- [111] BL Burrows and DJ Colwell. “The Fourier transform of the unit step function”. In: *International Journal of Mathematical Education in Science and Technology* 21.4 (1990), pp. 629–635.
- [112] Xavier Bertou et al. “Calibration of the surface array of the Pierre Auger Observatory”. In: *Nuclear Instruments and Methods in Physics Research Section A: Accelerators, Spectrometers, Detectors and Associated Equipment* 568.2 (2006), pp. 839–846.
- [113] Alan Coleman. “The new trigger settings”. GAP 2018-001.
- [114] Pierre Billoir. “Proposition to improve the local trigger of Surface Detector for low energy showers”. GAP 2009-179.
- [115] David Nitz. “Trigger comissioning”. Auger Collaboration Meeting. Mar. 2023.
- [116] Quentin Luce. “Comparing UB and UUB data: station-level differences in simulated events”. Auger Collaboration Meeting. Mar. 2023.
- [117] David Nitz. “Surface Detector Trigger Operating Guide”. GAP 2006-057.
- [118] Pierre Billoir. “Peak Searching in FADC traces”. GAP 2002-076.
- [119] Laura Molina Bueno, Pierre Billoir, and Ioana Maris. “Signal variance for the TOTd and MoPS triggers”. GAP 2002-076.